Article   https://doi.org/10.1038/s41467-024-52809-1

The G4 resolvase Dhx36 modulates cardiomyocyte differentiation and ventricular conduction system development

Pablo Gómez-del Arco [1,2,3] ✉, Joan Isern [4,5], Daniel Jimenez-Carretero [6], Dolores López-Maderuelo [2,16], Rebeca Piñeiro-Sabarís [3,7], Fadoua El Abdellaoui-Soussi [1,2,17], Carlos Torroja [6], María Linarejos Vera-Pedrosa[8], Mercedes Grima-Terrén [4,5], Alberto Benguria [9], Ana Simón-Chica [10], Antonio Queiro-Palou [1,2,18], Ana Dopazo [9], Fátima Sánchez-Cabo [6], José Jalife[8,11], José Luis de la Pompa [3,7], David Filgueiras-Rama [3,10,12], Pura Muñoz-Cánoves [4,5,13,14] ✉ & Juan Miguel Redondo [2,3,15] ✉

Extensive genetic studies have elucidated cardiomyocyte differentiation and associated gene networks using single-cell RNA-seq, yet the intricate transcriptional mechanisms governing cardiac conduction system (CCS) development and working cardiomyocyte differentiation remain largely unexplored. Here we show that mice deleted for *Dhx36* (encoding the Dhx36 helicase) in the embryonic or neonatal heart develop overt dilated cardiomyopathy, surface ECG alterations related to cardiac impulse propagation, and (in the embryonic heart) a lack of a ventricular conduction system (VCS). Heart snRNA-seq and snATAC-seq reveal the role of Dhx36 in CCS development and in the differentiation of working cardiomyocytes. *Dhx36* deficiency directly influences cardiomyocyte gene networks by disrupting the resolution of promoter G-quadruplexes in key cardiac genes, impacting cardiomyocyte differentiation and CCS morphogenesis, and ultimately leading to dilated cardiomyopathy and atrioventricular block. These findings further identify crucial genes and pathways that regulate the development and function of the VCS/Purkinje fiber (PF) network.

The heart, one of the earliest developing organs in mammals, plays a crucial role in supplying nutrients and oxygen to the growing embryo. The heartbeat relies on the specialized cardiomyocytes within the cardiac conduction system (CCS) that rapidly propagate the cardiac impulse to the working myocardium. The CCS comprises the heart´s natural pacemaker, or sinoatrial node (SAN), along with three interconnected structures: the atrioventricular node (AVN), the His bundle, and the right and left bundle branches integrated within the Purkinje system. These meticulously arranged components facilitate rapid and uniform propagation of cardiac impulses, ensuring synchronized

ventricular excitation leading to efficient contraction. The specialized CCS as well as the entire development and morphogenesis of the heart represent a continuous process that extends beyond the embryonic stages, culminating in the early neonatal period.

Despite substantial knowledge, our understanding of the transcriptional and posttranscriptional mechanisms governing heart and CCS development and function remains incomplete[1]. In this study, we investigated the role of specific nucleic acid secondary structures in mammalian heart development and function, centering particularly on the differentiation of working and CCS cardiomyocytes. We focused

on guanine-rich nucleic acid structures (G-quadruplexes; G4) present in DNA (dG4) and RNA (rG4), which play roles in a variety of vital processes[2]. These G4 structures are resolved by Dhx36, a highly conserved member of the DExD/H box helicase family (also called Rhau [RNA associated with AU-rich element] and G4R1 [G4 resolvase 1])[3]. The G4 resolvase action of Dhx36 alters how G4 structures influence DNA- and RNA-dependent processes, thereby regulating transcription and translation[4,5]. The essential developmental role of Dhx36 is highlighted by embryonic lethality following germline *Dhx36* deletion in mice[6].

Dhx36 is one of the few helicases known to resolve rG4s and has been implicated in the posttranscriptional regulation of mRNAs in the cytoplasm of cardiomyocytes, affecting both transcript stability and translation[7]. For instance, Dhx36 regulates *Nkx2-5* RNA stability through its interaction with AU-rich regions in the mRNA 3´ UTR, and its translation by resolving a G4 structure present in its 5´ UTR region[8]. The lack of *Dhx36* in the heart has been shown to affect the stability and translation of other mRNAs, such as *Hexim1, Hey2* or *Yap1*[9,10], yet its direct involvement in transcriptional regulation remains largely unexplored, despite its ability to resolve dG4s[3].

Recent studies investigating cardiac cell populations during murine regenerative periods, in postnatal days (PD)0 to PD8, post-infarction at the single-cell level have provided valuable insight into the various resident cardiac cells, their distinctive molecular signatures, and the dynamic changes that occur during the regenerative phase[11,12]. Among these cell clusters, cardiomyocytes typically comprise less than 50% of the heart cells. Other major cell types in the heart include fibroblasts and endothelial cells (both coronary and endocardial). Less abundant populations include immune cells (mainly macrophages and lymphocytes), smooth muscle cells, pericytes, epicardial cells and neural cells[11,12].

Bulk RNA-seq studies can be challenging when trying to discern the influence of a specific gene whose deletion is conditionally limited to a subset of cells. To address these challenges, scRNA-seq and single-cell ATAC-seq (scATAC-seq) have proven to be valuable tools for understanding the transcriptional landscapes and how the conditional deletion of a specific gene affects the chromatin accessibility. These technologies have elucidated the transcriptional networks regulating the differentiation and function of the different cardiac cell types, both in healthy and pathological conditions[11–19]. Additionally, they have contributed to a better understanding of the development and function of the CCS in both mice and humans[20–24]. For instance, initial studies delineated early developmental populations by identifying progenitor cells expressing *Nkx2-5* and *Isl1*, characterizing cell types specific to different zones and their associated molecular signatures[16].

This study underscores the critical role of Dhx36 in resolving dG4 structures within cardiomyocytes, governing the transcriptional regulation of essential genes involved across diverse signaling pathways. This activity is pivotal to heart homeostasis and the development of the CCS. Furthermore, in addition to CCS development, Dhx36 significantly affected the differentiation of working cardiomyocytes, which are crucial for heart function. These effects eventually manifested as overt signs of PR and QRS complex prolongation, preceding advanced atrioventricular block events in the context of overt signs of cardiomyopathy.

Results

Dhx36 deficiency induces dilated cardiomyopathy and sudden cardiac death

In a previous study, we deleted *Dhx36* in mature skeletal muscle using the myocyte-specific driver *MCK-Cre*[25,26]. The *Dhx36^{floxed} (Dhx36^{f/f}); MCK^{Cre/wt} (Dhx36^{ΔMCK-Cre})*[27] mice became sick and developed a severe phenotype. As the *MCK-Cre* allele is also active in the myocardium, we inferred that the observed illness likely resulted from co-deletion of *Dhx36* in the heart, likely leading to sudden death due to heart failure.

Supporting this conclusion, we found that *Dhx36^{ΔMCK-Cre}* mice exhibited dilated cardiomyopathy with significant heart enlargement (Supplementary Fig. 1a, b).

To clarify the putative roles of Dhx36 in the heart, we initially analyzed the expression of the protein in embryonic and adult hearts by immunohistochemistry (IHC) (Fig. 1a, b). Consistent with an earlier report[8], Dhx36 protein expression was much higher in the fetal than in the adult hearts. During development, Dhx36 expression peaked at embryonic day 11.5 (ED11.5), with the protein expressed in cardiomyocytes in both atria and ventricles (Fig. 1a). Dhx36 expression was reduced by ED12.5 and was maintained preferentially in trabecular cardiomyocytes (Fig. 1a, i). In adult hearts, Dhx36 was scarcely detectable by IHC except within the atria (Fig. 1b, ii). Western blot analysis of subcellular fractions of total adult mouse hearts detected Dhx36 in both the nucleus and (to a lesser degree) the cytoplasm (Fig. 1c), suggesting that Dhx36 may control mRNA processing, translation, and transcription within cardiomyocytes. Finally, IHC analysis in ED12.5 hearts confirmed Dhx36 expression in the cytoplasm and nuclei of right and left ventricular cardiomyocytes in wild-type (WT) embryos but not in *Dhx36^{f/f};Nkx2-5^{Cre/wt}* (*Dhx36^{Nkx2-5}*) mutant embryos (Fig. 1d).

To analyze the cardiac-restricted roles of Dhx36, we crossed the *Dhx36^{floxed}* line with two well-known (purely cardiac) myocyte *Cre* transgenic strains, driven by regulatory elements from the cardiac *Troponin T* (*cTnT-Cre/Tnnt2-Cre*)[28] locus or the cardiac alpha myosin heavy chain (*αMHC-Cre/Myh6-Cre*)[29] locus. While *Myh6-Cre* recombination is predominantly restricted to perinatal cardiomyocytes[29], the *Tnnt2-Cre* allele is expressed from ED8.0 onwards exclusively in differentiating cardiomyocytes, and its specific expression is maintained in all cardiomyocytes during adulthood[28].

Dhx36^{f/f};Tnnt2^{Cre/wt} (*Dhx36^{Tnnt2}*) mice survived birth but succumbed at 3 weeks postpartum, with no mutant surviving beyond 10 months (ID$_{50}$ ≈ 4 months) (Fig. 2a). Young mutant mice (2- to 3-week-old) exhibited rounded hearts and enlarged (dilated) atria as compared to their WT counterparts. Histological analysis showed prominent dilated cardiomyopathy, characterized by thin compact ventricular walls, left-ventricular non-compacted (LVNC) myocardium, a thin ventricular septum, dilated atria, and interstitial fibrosis (Fig. 2b, c). Echocardiography studies revealed defective contraction in *Dhx36^{Tnnt2}* mutant mice as compared to WT, along with increased left ventricular end-diastolic (LVd) volumes, indicative of dilated cardiomyopathy (Fig. 2d). Electrocardiogram (ECG) analyses showed overt prolongation of the PR interval and the QRS complex in *Dhx36^{Tnnt2}* mutant mice (Fig. 2e), suggesting compromised cardiac impulse propagation at various levels. Furthermore, the reduced amplitude of the QRS complex in *Dhx36^{Tnnt2}* mutant mice indicated the influence of the underlying pathophysiological substrate on heart electrical signals (Supplementary Data 1 for ECG parameter measures).

To study the role of Dhx36 in adult cardiac homeostasis, we deleted the gene in an α-*MHC-Cre* (*Myh6^{Cre/wt}*) mouse line, which is characterized by Cre expression under the control of the alpha-myosin heavy chain promoter, with peak perinatal activity occurring in postnatal pups immediately after birth[29]. In *Dhx36^{f/f};Myh6^{Cre/wt}* (*Dhx36^{Myh6}*) mice, premature death started later, although at a higher rate than in *Dhx36^{Tnnt2}* mutants (Fig. 2f). *Dhx36^{Myh6}* mice displayed early atrial dilatation and extensive cardiac fibrosis without signs of left ventricular noncompacted (LVNC) myocardium (Fig. 2g). Echocardiography studies depicted a significant decrease in left ventricular ejection fraction (LVEF) and an increase in LVd volume (Fig. 2h), similar but stronger to the dilated cardiomyopathy phenotype observed in *Dhx36^{Tnnt2}* mutant mice (Fig. 2d). However, unlike *Dhx36^{Tnnt2}*, *Dhx36^{Myh6}* mutants did not exhibit statistically significant alterations of ECG parameters related to cardiac impulse propagation (PR interval and QRS complex duration) as compared with WT (Fig. 2i, and Supplementary Data 1). The QRS complex amplitude in *Dhx36^{Myh6}* mice was also not significantly
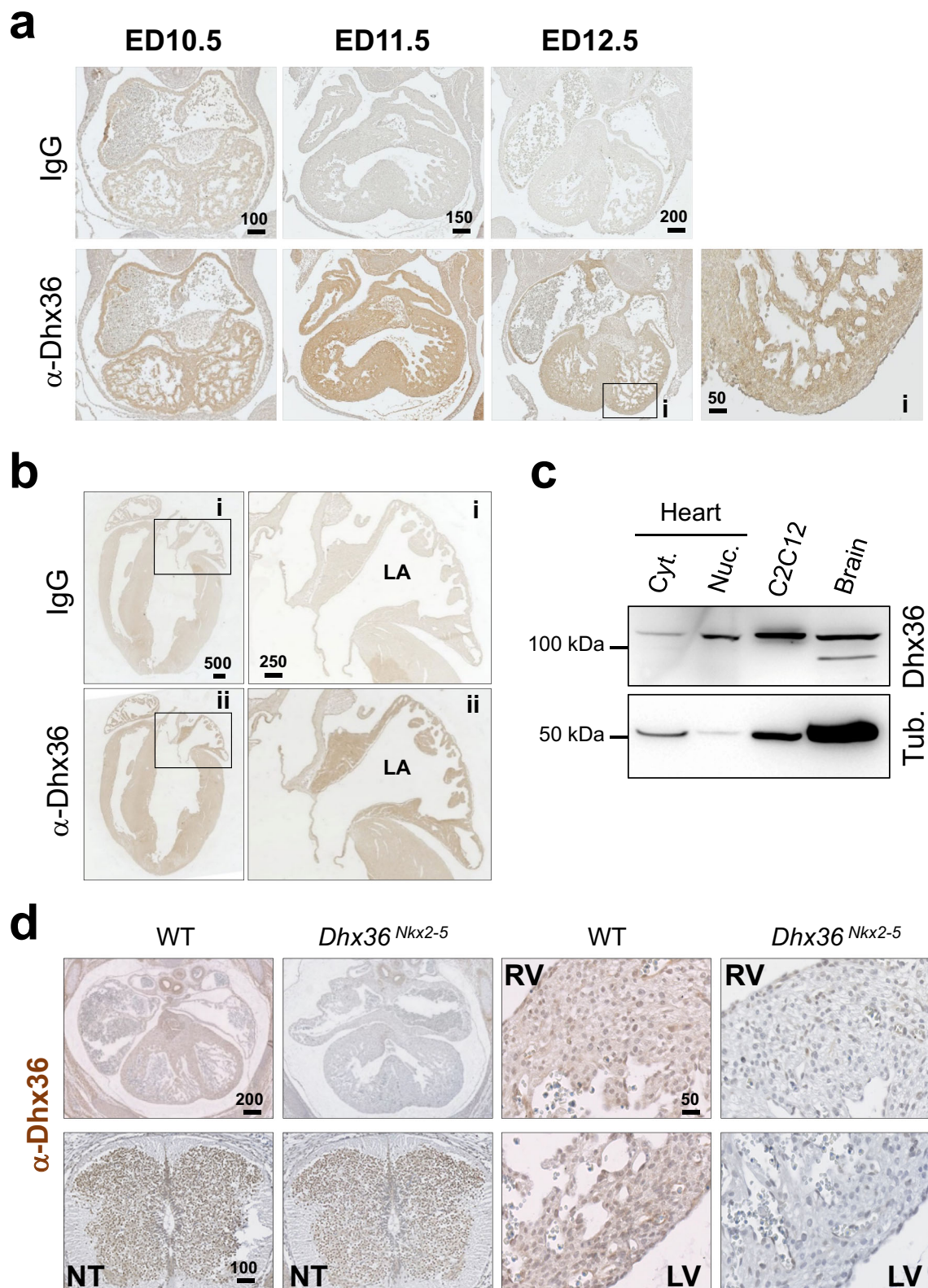
different compared to WT (Fig. 2i), consistent with the absence of signs of LVNC myocardium in Dhx36*Myh6* mutants.

Interestingly, neither Dhx36*Tnnt2* nor Dhx36*Myh6* mutant mice showed significant changes in the average heart rate over 60-s ECG recordings compared to WT (Fig. 3a, b). However, a more detailed analysis of the ECG tracings revealed a higher incidence of various paroxysmal arrhythmic events in the mutant lines than in the WT.

Specifically, Dhx36*Tnnt2* mutant mice showed a significantly higher number of relevant AV block events (e.g., 2:1 AV conduction, Mobitz II/advanced, or complete AV block) than WT or Dhx36*Myh6* mutants (Fig. 3c, d). Moreover, Dhx36*Tnnt2* mutants also showed overt signs of sinus node dysfunction, which were not documented in WT or Dhx36*Myh6* mutants (Fig. 3e, f, g), indicating further signs of defective cardiac impulse generation in Dhx36*Tnnt2* mutants. Ventricular

Fig. 1 | Dhx36 protein expression in embryonic and adult hearts.
a Immunohistochemical (IHC) analysis of ED10.5, ED11.5, and ED12.5 embryonic hearts stained with IgG (upper panels) or α-Dhx36 (lower panels). Panel i presents a magnified view of a specific region (boxed area) within the left ventricle of an ED12.5 heart. **b** IHC staining of adult hearts with IgG (left upper panel) or α-Dhx36 (left lower panel). Panels i and ii show magnified views of the corresponding boxed areas. **c** Western blotting showing Dhx36 expression in cytoplasmic (Cyt.) and nuclear (Nuc.) subcellular compartments of total adult hearts. Specific expression was validated by analyzing total extracts of C2C12 myocytes and mouse brain. Anti-tubulin (Tub.) was blotted in the same membrane after α-Dhx36 and served as a

cytoplasmic control. Samples derived from the same experiment. **d** IHC of Dhx36 expression in WT and *Dhx36* $^{Nkx2-5}$ ED12.5 embryonic hearts (top left panels). The right panels depict magnifications of regions of the right ventricles (RV, top) or left ventricles (LV, bottom). As a control for Dhx36 staining, the bottom left panels show IHC in the neural tube of the same WT and *Dhx36* $^{Nkx2-5}$ embryos. All micrographs and western blots shown are representative of three independent experiments rendering similar results. Uncropped blot for Fig. 1c is provided in the Source data file. Scale bars are expressed in μm and apply to corresponding images, as they present the same magnifications.
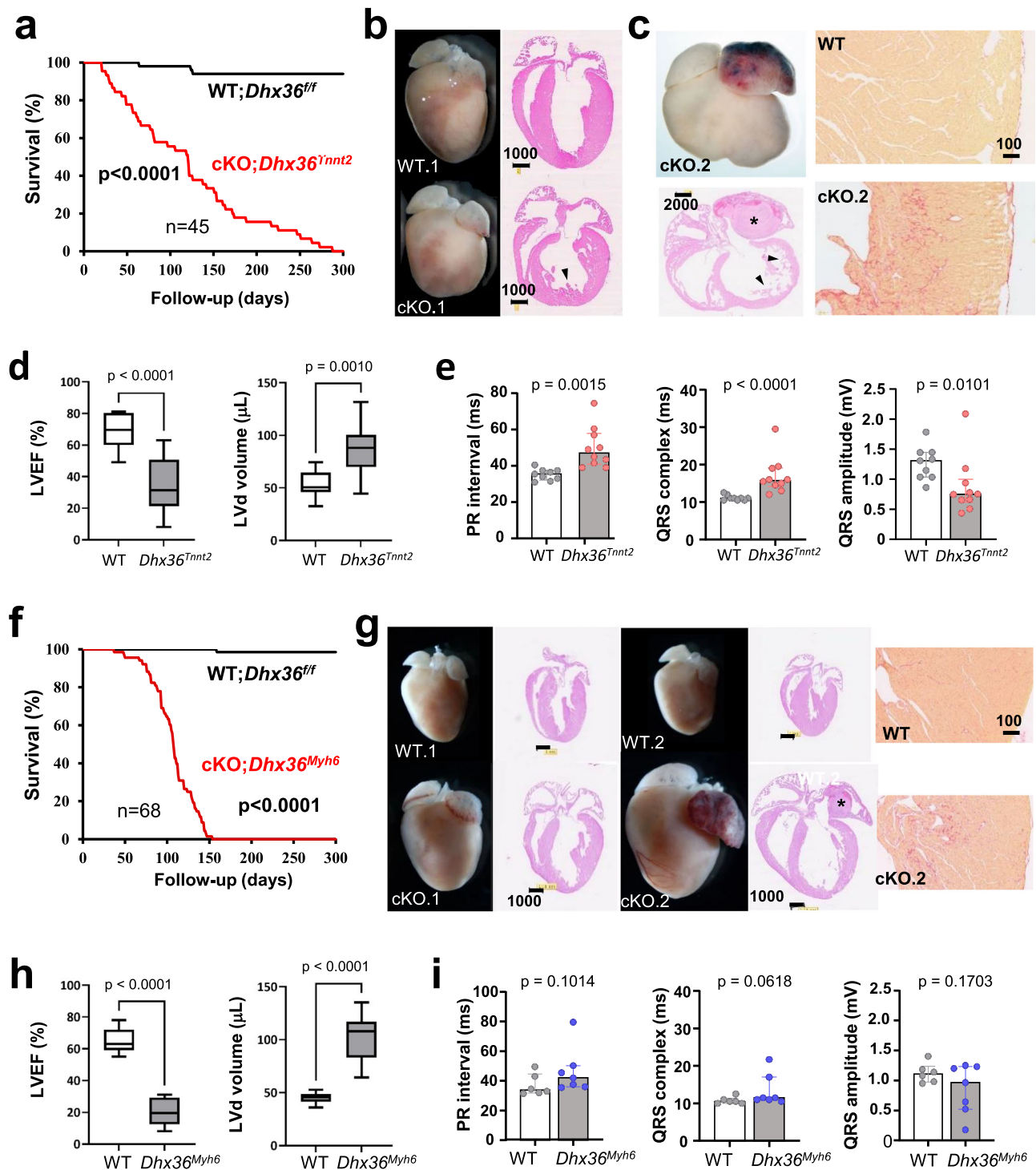
Fig. 2 | *Dhx36* deletion induces dilated cardiomyopathy, reduced ejection fraction, and surface ECG alterations. a Kaplan-Meier survival curve comparing WT mice (*Dhx36*^*f/f*) with *Dhx36*^*Tnnt2* mutant mice. **b** Gross morphology of hearts from 21-day-old WT (top left) and *Dhx36*^*Tnnt2* conditional KO (cKO.1) mice (bottom left). Right panels show hematoxylin & eosin (H&E)-stained sections of the corresponding hearts. **c** Left panels: a 90-day old *Dhx36*^*Tnnt2* mouse (cKO.2) exhibiting overt signs of dilated cardiomyopathy and non-compaction of the left ventricular (LV) myocardium. The left atrium displays a prominent thrombus in the H&E-stained section. Right panels: picrosirius red stained sections highlight larger LV fibrotic areas (lower) compared to representative WT (upper) sections. The pictures in **b** and **c** are representative of 5 and 3 independent experiments, respectively, analyzing WT and mutant hearts of around similar ages, all showing similar phenotypes. **d** Box plots representing the distribution of IQR values for LV ejection fractions (LVEF; left) and the LV end-diastolic (LVd) volumes (right) of *Dhx36*^*Tnnt2* mutant mice ($n = 10$) and WT ($n = 10$). Lower and upper hinges of the boxes correspond to Q1 and Q3 (25th and 75th percentiles), with the median represented by the horizontal line inside the box, while whiskers extend from hinges to minima and maxima values. The exact values of all these data are annotated in the Source Data

file. **e**, Comparisons of PR interval (left), QRS complex duration (middle), and amplitude (right) between *Dhx36*^*Tnnt2* mutant mice ($n = 10$) and WT ($n = 9$). **f** Kaplan-Meier survival curve comparing WT mice (*Dhx36*^*f/f*) with *Dhx36*^*Myh6* mutant mice. **g** Same analysis as in **b** and **c** but of hearts from WT and *Dhx36*^*Myh6* mutant mice aged 40 days (cKO.1) or 82 days (cKO.2). The cKO.2 heart exhibited a large thrombus in the left atrium. The pictures shown are representative of 4 and 3 independent experiments, respectively, analyzing WT and mutant hearts of similar ages, all showing similar phenotypes. **h**. Box plots comparing (as in **d**) LVEFs (left) and LVd volumes (right) between *Dhx36*^*Myh6* mutant mice ($n = 10$) and WT ($n = 9$). The values are represented in the Source Data file. **i** Comparisons of PR interval (left), QRS complex duration (middle), and amplitude (right) between *Dhx36*^*Myh6* mutant mice ($n = 7$) and WT ($n = 6$). Asterisks indicate left atrial thrombi, and arrowheads show myocardial areas with non-compacted trabeculae. No phenotypic differences were observed between sexes (sex of the mice are annotated in the Source Data file). Significance was determined using unpaired two-sided *t*-test, except for **a** and **f**, in which a χ^2 was used. *p*-values are shown in the corresponding figures. Source data for **d**, and **h** are provided in the source data file and in Supplementary Data 1 for **e** and **i**. Scale bars are as in Fig. 1.

arrhythmia in the form of premature ventricular complexes was also documented with a higher incidence in *Dhx36*^*Tnnt2* mutants than in *Dhx36*^*Myh6* mutant mice and WT (Fig. 3h). There were also instances of nonsustained episodes compatible with bidirectional ventricular tachycardia (Fig. 3i), characterized by bifocal ectopic origin in the Purkinje fiber network[30]. In contrast, WT did not show any ventricular arrhythmia during the ECG recordings.

Some of the oldest *Dhx36*^*Tnnt2* and *Dhx36*^*Myh6* mutant mice showed left atrial thrombosis (Fig. 2c, g). Indeed, in animals with overt signs of end-of-life conditions ($n = 6/6$), macroscopic analysis after euthanasia revealed the presence of thrombi in the left atrium. In one heterozygous mouse, a thrombus was also observed in the left ventricle ($n = 1/7$) (Supplementary Fig. 1c). Left atrial thrombi were also detected in postmortem examinations ($n = 2/3$) of mice that died before they could undergo in-vivo examination (Supplementary Fig. 1d). These results indicate a significant degree of atrial and ventricular cardiomyopathy favoring thrombus formation in both mutant lines.

The detection of Dhx36 in embryonic trabecular myocardium, its persistence (albeit at low levels) in the postnatal atrial myocardium (Fig. 1), and some loss-of-function cardiac phenotypes suggested that Dhx36 might regulate specific target genes implicated in CCS morphogenesis, and ultimately in myocardial contractility. Moreover, these data also pointed to Dhx36 as a crucial regulator of cardiomyocyte differentiation and postnatal heart homeostasis.

Dhx36 controls cardiac conduction system morphogenesis

The CCS is crucial for the effective synchronization of contractile function through normal and rapid impulse propagation. We thus analyzed mutant hearts to elucidate the impact of *Dhx36* deficiency on CCS morphogenesis. We initially considered using the *Cx40-eGFP* Knock-In (*ki*) reporter line (see Methods) to check the ventricular Purkinje fiber (PF) network organization[31]. Unfortunately, *Gja5* (*Cx40*) and *Dhx36* loci are located in close genomic proximity to each other on mouse chromosome 3; consequently, generating a *Dhx36*^*cKO*;*Cx40-eGFP* compound mutant was unfeasible. We, therefore, examined VCS architecture in conditionally deficient *Dhx36* hearts using whole-mount immunostaining of the pan-VCS marker Cntn2. In WT hearts, Cntn2 is uniformly expressed throughout the VCS; however, in *Dhx36*^*Myh6* hearts, the VCS is hypoplastic, with thinner Purkinje fibers and a less intricate network (Fig. 4a). This underdeveloped pattern suggested a postnatal morphogenic defect during the final stages of CCS growth, specifically from PD0 to PD7. In contrast, in *Dhx36*^*Tnnt2* mice, *Dhx36* deletion occurs at embryonic stages, which may increase the deleterious effects on VCS development. Hearts from *Dhx36*^*Tnnt2* mice showed no detectable Cntn2

immunoreactivity, suggesting complete atresia of the ventricular Purkinje fiber network (Fig. 4b). This apparent VCS agenesis correlated with a more severe ECG phenotype than otherwise observed in these mutant mice (Figs. 2 and 3).

To investigate whether CCS development and maturation are impaired in *Dhx36*^*Tnnt2* mutants, we performed in situ hybridization (ISH) analysis on ED16.5 and PD7 mutant hearts. This analysis revealed that the expression of VCS markers *Etv1*, *Gja5*, *Slit2* and *Irx3* were downregulated in ED16.5 mutant hearts (Supplementary Fig. 2a–d), while the expression of *Anf* (*Nppa*) remain relatively unaffected (Supplementary Fig. 2e). In contrast, *Nrg1* was upregulated at ED16.5, suggesting a potential compensatory response (Supplementary Fig. 2f). These findings were corroborated in PD7 *Dhx36*^*Tnnt2* mutant hearts, which also exhibited reduced *Hcn4* expression (Fig. 4c–g), stable *Irx3* levels, and expanded *Anf* transcription (Supplementary Fig. 2g, h). Together, these results indicate that CCS development and maturation are compromised in *Dhx36*^*Tnnt2* mutants.

Dhx36 regulates the transcription of the cardiac conduction system gene program

To gain insight into the molecular mechanisms underlying the electrophysiological phenotypes observed in *Dhx36*-deficient adult mice, we conducted bulk RNA sequencing (RNA-seq) on whole hearts from young mice (2- to 3-weeks old), before the worsening of the cardiac phenotype. This analysis revealed 703 upregulated transcripts (238 ≥ 2.0-fold change) and 354 downregulated transcripts (100 ≤ 2.0-fold change) in *Dhx36*^*Myh6*-deficient mice as compared to WT mice (Supplementary Data 2). Given our primary interest in the role of Dhx36 in gene transcription, we focused on downregulated genes using the Enrichr platform[32]. Gene ontology (GO) analysis of biological processes[33,34] identified significant depletion in categories related to cardiac muscle cell action potential and cation, potassium, and sodium transport (Supplementary Fig. 3a). Molecular function analyses highlighted depletion in genes associated with inward rectifier and voltage-gated potassium channel activity, along with atrial fibrillation and rare diseases such as Brugada syndrome (Supplementary Fig. 3b). Most of the depleted genes that participate in cardiac impulse generation or propagation, including *Hcn4, Kcne1, Kcnd2*, and *Kcnv2*, had reduced expression (Supplementary Fig. 3c). These results support a role for Dhx36 in controlling normal cardiomyocyte physiology at multiple levels, particularly electrical conductance maturation, CCS morphogenesis and function.

We next validated the most relevant altered genes identified in the transcriptomic analysis using RT-qPCR on the same samples used for the RNA-seq pools (Supplementary Fig. 3d). The analysis confirmed prominent upregulation or downregulation of several CCS genes in
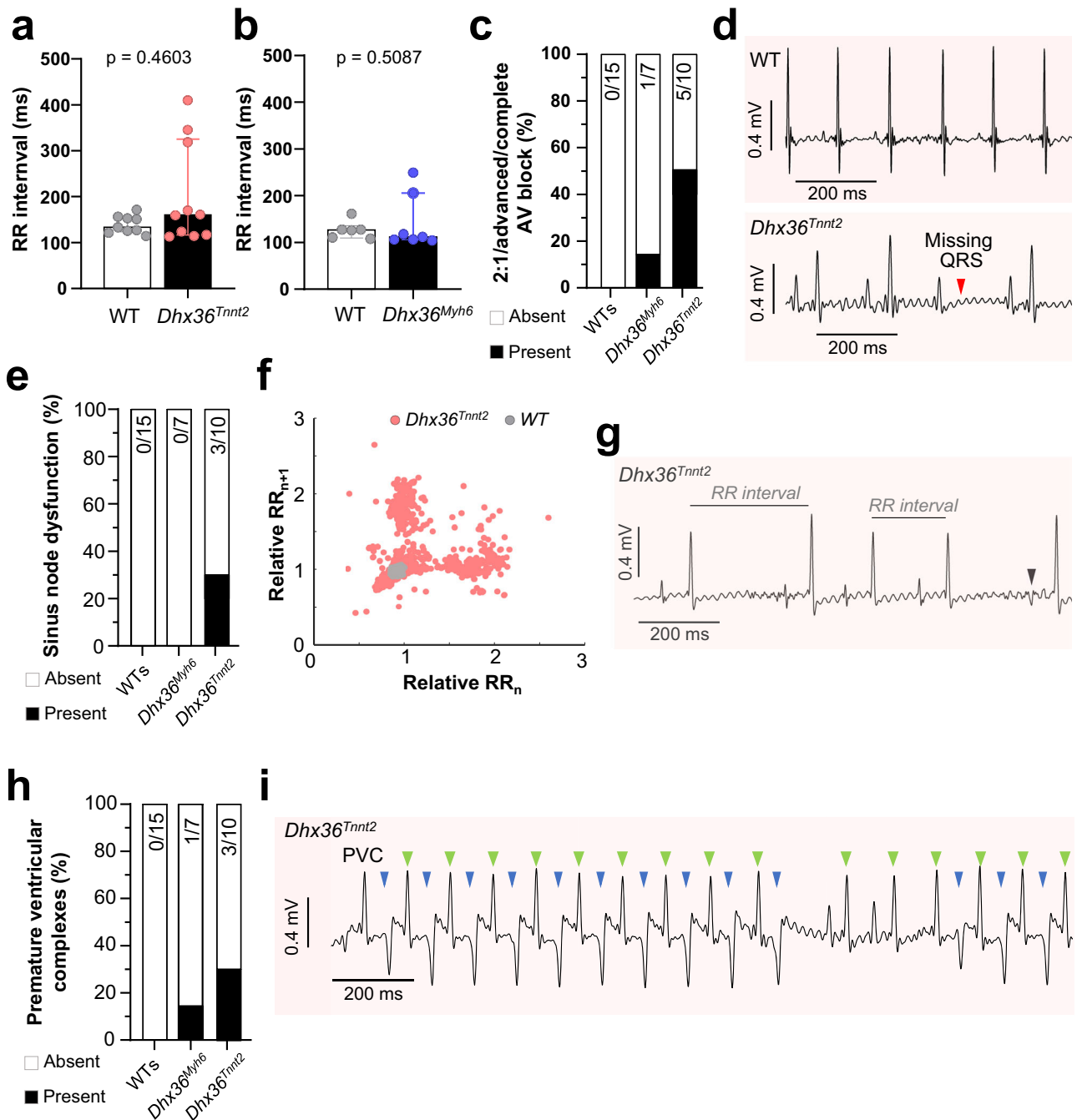
Fig. 3 | *Dhx36* deletion increases abnormal paroxysmal arrhythmic events.
a, b Comparative analysis of RR intervals (heart rate calculated as [1000/RR interval in ms] x 60) between *Dhx36^Tnnt2^* mutant mice and WT (**a**), and *Dhx36^Myh6^* mutants and WT (**b**). **c** Incidence of relevant atrioventricular (AV) block events during ECG recordings of WT mice and *Dhx36^Tnnt2^* and *Dhx36^Myh6^* mutant mice. **d** Representative ECG tracings depicting a WT mouse and a *Dhx36^Tnnt2^* mutant mouse with a paroxysmal AV block event. **e** Incidence of sinus node dysfunction during ECG recordings in WT mice and *Dhx36^Tnnt2^* and *Dhx36^Myh6^* mutant mice. **f** RR variability representation of *Dhx36^Tnnt2^* mice (in light red) as compared to WT mice (in grey). Each dot represents a RR interval. **g** Sample tracing with overt signs of sinus node dysfunction (arrowhead) during the ECG recording of a *Dhx36^Tnnt2^* mutant mouse.

h Incidence of premature ventricular complexes (PVC) during ECG recordings in WT mice and *Dhx36^Tnnt2^* and *Dhx36^Myh6^* mutant mice. **i** Sample tracing of a potential nonsustained bidirectional ventricular tachycardia episode in an ECG recording of a *Dhx36^Tnnt2^* mutant mouse. Green arrowheads show one PVC morphology, probably from Purkinje fibers at the root of the His-Purkinje system, and blue arrowheads show a second PVC morphology, in the absence of overt P waves. In panels **c, e**, and **h**, WT mice were grouped, as they did not exhibit any significant cardiac rhythm alterations. The mice analyzed were the same that in Fig. 2e, i. Statistical significance was determined using unpaired two-sided *t*-test (**a** and **b**) and the data are presented as mean ± SEM. The source data are provided in the Source data file and Supplementary Data 1.

*Dhx36^Myh6^* mice; for example, *Hcn4* and *Kcne1* were downregulated 2.0 and 2.27-fold, respectively (Supplementary Fig. 3d).

Given the marked electrophysiological defects and reduced transcriptional expression of CCS genes in *Dhx36^Myh6^* mice, we extended our analysis to other CCS transcriptional regulators and structural/

functional proteins, including *Etv1, Gja5, Cntn2, Cpne5, Pcp4*, and *Sema3a*. Alterations in transcripts encoding contactin2 (*Cntn2*; 2.7-fold reduction) and the Purkinje cell protein 4 (*Pcp4*; 5-fold reduction) were detected, while *Gja5 (connexin 40)*, and *Cpne5* remain unchanged, possibly due to their expression in cardiac cells other than
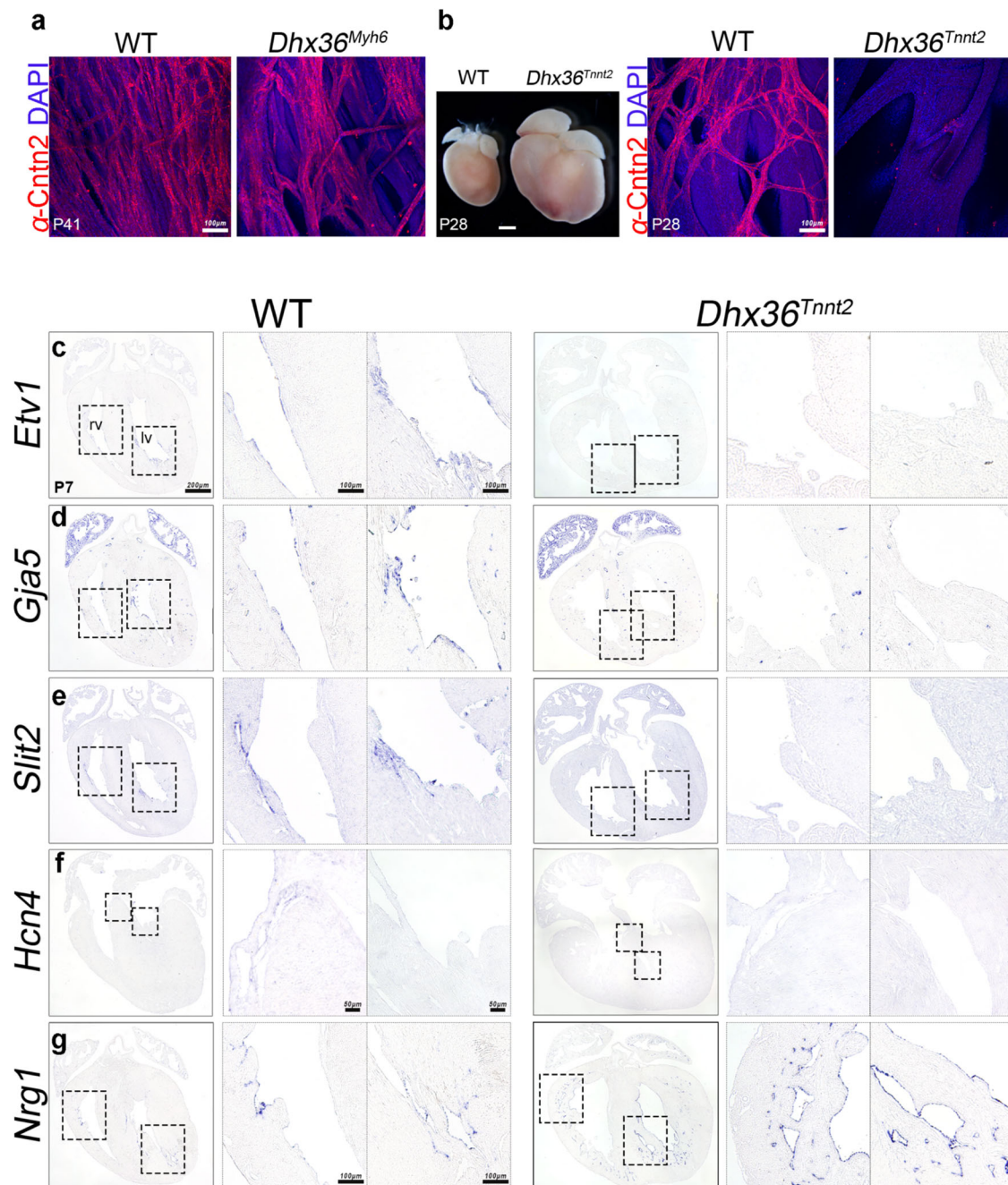
Fig. 4 | Impact of perinatal and embryonic *Dhx36* deletion on CCS morphogenesis. a Whole-mount (WM) confocal immunofluorescence (IF) of hearts of 41-day-old (PD41) WT and *Dhx36^Myh6^* littermates, revealing an underdeveloped ventricular conduction system/Purkinje fiber (VCS/PF) network in the mutant. The pictures are representative of 3 independent experiments, analyzing WT and mutant hearts of similar ages, all rendering similar results. **b** Left: gross morphology of hearts from PD28 WT and *Dhx36^Tnnt2^* littermates. Right: WM confocal IF of the same hearts, indicating an undetectable VCS/PF network in the mutant. Representative images are presented from a total of three *Dhx36^Myh6^* and five *Dhx36^TnnT2^* analyzed mutants. The pictures are representative of 5 independent experiments, analyzing WT and mutant hearts of similar ages, all rendering similar results. **c–g** ISH analysis of PD7 (P7) wild type and *Dhx36^Tnnt2^* hearts hybridized with various CCS markers. Representative images are shown, three wild type and mutant embryos were examined; rv, right ventricle; lv, left ventricle. Scale bars, 100 μm in **a**, **b** (confocal images), 1 mm in **b** (whole hearts images). 200 μm in (**c–g**, general heart views), 100 μm in (**c**, **d**, **e**, **g**, high magnification views), and 50 μm (**f**, high magnification, showing *Hcn4* staining in the AVN). The depicted scale bars are valid for both corresponding WT and mutant pictures.

cardiomyocytes (Supplementary Fig. 3e). For example, the stability of *Gja5* may reflect the expression of Connexin 40 (Cx40) not only in the CCS but also in atrial cardiomyocytes and coronary arteries as shown in Fig. 4, Supplementary Fig. 4 and subsequent sections.

To explore the potential direct transcriptional targets of Dhx36, we assessed the expression of selected genes in newborn *Dhx36^Myh6^* mice by qPCR. *Cntn2 and Kcne1* emerged as the sole transcripts showing a tendency towards reduced expression

($p = 0.071$ and $p = 0.0508$, respectively) (Supplementary Fig. 4a). In contrast, qPCR analysis of newborn *Dhx36^Tnnt2^* mutant pups (with *Dhx36* deletion during embryogenesis) showed substantial downregulation of *Hcn4* (2.5-fold), *Kcne1* (4.0-fold) and *Cntn2* (6.6-fold), indicating that these genes might be direct targets of Dhx36 or be reflective of CCS hypoplasia in these mutant mice (Supplementary Fig. 4b), in agreement with our ISH data (Fig. 4c–g and Supplementary Fig. 2).

Multiomic profiling of neonatal WT and mutant hearts

To comprehensively understand the regulatory landscape and gene expression patterns governed by Dhx36 across various heart cell populations, we employed single-nucleus multiome data (snATAC-seq and snRNA-seq). These datasets enabled us to integrate RNA expression and chromatin accessibility information from individual nuclei of different heart cell types in WT and *Dhx36^Tnnt2* mutant hearts at PD7. This time point corresponds to the critical VCS/Purkinje fiber (VCS/PF) period of differentiation within the first week after birth, during which the heart maintains its regenerative capacity and completes CCS formation.

Notably, *Dhx36^Tnnt2* mutant hearts at PD7 already exhibited signs of cardiac hypertrophy and CCS hypoplasia, reflecting a pronounced stress (Supplementary Fig. 5a). Median UMI and genes per cell values, as well as high-quality ATAC fragments per cell, were comparable between WT and conditional knockout (*Dhx36^Tnnt2*) (Supplementary Fig. 5b; see Methods). Our analysis revealed a significant transcription start site (TSS) enrichment score, indicating a closer chromatin landscape in *Dhx36^Tnnt2* cardiomyocytes (Supplementary Fig. 5c).

Multiomic analyses revealed the presence of up to 11 distinct resident cardiac cell types in both WT (Fig. 5a) and *Dhx36^Tnnt2* (Supplementary Fig. 6a) samples. Interestingly, *Dhx36* mRNA expression was detected across all WT cell types, with the highest expression observed in pericytes and B cells (Fig. 5b, c). The composition of cardiac cell populations was consistent between WT and *Dhx36^Tnnt2* nuclei, as demonstrated by UMAP representations (Fig. 5d) and were further characterized using established cell type–specific markers[11] (see comprehensive list, Supplementary Data 3; highlighted in the UMAP chart, Fig. 5a). Remarkably, UMAP representations of separated WT and *Dhx36^Tnnt2* KO samples revealed significant distinctions only in cardiomyocyte populations (Fig. 5d). Approximately 47% of the total cell population consisted of cardiomyocytes (Fig. 5e), while stromal/fibroblasts accounted for 23.5%, and endothelial cells constituted 16.4%. Among the latter, endocardial cells comprised 8.8%, and coronary artery endothelial cells made up 7.6%. Less prevalent cell types included epicardial cells, mural/pericytes, and mural/smooth muscle cells (Fig. 5e). Immune cells, such as myeloid cells, macrophages, T and B cells, and neural/glial-like cells, were also identified (Supplementary Fig. 6b, and Supplementary Data 3 for specific cell–type gene markers).

Analysis of knockout (KO) hearts indicated a similar representation of cell types within the sequenced nuclei as observed in WT hearts (Fig. 5). However, endothelial cells (16.1% and 15.7%) and fibroblasts (31.7%) in KO hearts exhibited increased percentages compared to WT, while KO cardiomyocytes displayed distinct gene expression profiles and chromatin accessibility landscapes, as evidenced in the multimodal UMAP plots (Figs. 5d, 6a and Supplementary Fig. 7a).

In young (PD7) hearts, a proliferation signature enriched in proliferation-related genes like *Mki67* was identified in specific cell types, including proliferating mural-like cells (pericytes), a subset of endothelial cells, and proliferating fibroblasts (Supplementary Fig. 7b and Supplementary Data 3). The population of proliferating fibroblasts (325 nuclei in KO vs. 183 in WT) and endothelial cells (196 in KO vs. 88 in WT) increased in mutant hearts, likely reflecting myocardial remodeling (Supplementary Fig. 7b).

Dhx36 regulates cardiomyocyte differentiation and VCS/Purkinje fiber morphogenesis

Our focus shifted to the cardiomyocyte populations in both WT and KO hearts (Fig. 6a), categorized based on the expression of key genes, including *Ttn* and *Ryr2* (Fig. 6b and Supplementary Data 3). Compared to previous work analyzing scRNA-seq of PD8 WT half ventricles[11], our PD7 WT hearts mirrored their five cardiomyocyte (CM) clusters, with an additional two more clusters (CM1 to CM7) emerging (Fig. 6a). The largest cluster, CM1, was defined by expression of genes like *Fgf13*, *Fhl2* and *Gm30382* (Fig. 6 and Supplementary Data 3). The less abundant CM2 consisted of cardiomyocytes (*Top2a* +, *Lockd* +, and *Cenpp* +*) with a proliferating profile, which is expected to decline after PD7, when most cardiomyocytes become post-mitotic (Supplementary Data 3). CM3 expressed pan-CM genes but also *Ddc* and *1700042O10Rik* transcripts (Fig. 6b and Supplementary Data 3). CM4 and CM5, associated with regenerative and injured non-regenerative hearts[11], were nearly absent, with CM4 expressing genes like *Sod2* and *Atp5b*, while CM5 expressing genes like *Xirp2*, *Ankrd1*, and *Enah*, which have been previously associated with non-regenerative injuries like myocardial infarction (MI) after PD7[11] (Fig. 6 and Supplementary Data 3).

Unlike the study by Cui et al.[11], our analyses utilized whole hearts, enabling us to identify a VCS/PF cell cluster (CM6) expressing lineage-specific genes like *Cntn2*, *Tbx3*, *Robo1*, *Cpne5*, *Sema3a*, and *Ncam1*. Additionally, a distinct cluster of atrial cardiomyocytes (CM7) was identified, confirmed by the expression of *Ryr3*, *Fgf12*, and *Tmem163*[15], among others (Fig. 6 and Supplementary Data 3). Differential expression analysis of the VCS/PF cluster as compared to the predominant WT CM1 cluster revealed new potential PF gene markers, including *Shisa9*, *Kirrel3*, *Slit2/3*, *Col4a3*, *Col4a4*, *Ephb1*, *Ntm*, *Grip1*, and *Plxdc2* (Fig. 6b and Supplementary Data 3, 4). Gene ontology analysis suggested the association of some of these genes (*Robo1*, *Slit2*, *Slit3*, *Sema3a*, *Sema3c*, and *Ephb1)* with axon guidance, possibly implicating them in PF network morphogenesis.

In contrast to WT, mutant hearts displayed only three distinct cardiomyocyte clusters: mCM7 (atrial), mCM2 (proliferating), and a unique mCM0 cluster, distinct from WT CM1 (Fig. 6a). The mCM2 population, similar to WT CM2, expressed cell cycle genes like *Top2a* (Fig. 6b), constituting a comparable proportion of total cardiomyocytes (2.63% in mutant vs. 2.15% in WT). Remarkably, mutant cardiomyocytes lacked a *dopa-decarboxylase* (*Ddc*)-expressing CM3 cluster, suggesting a role of Dhx36 in the differentiation of this specific cardiomyocyte type (Fig. 6).

The mCM0 cluster, predominant among mutant cardiomyocytes, expressed genes found in the WT CM1 and CM5 clusters, but not in the WT CM2, CM3, or CM4 clusters. Genes in mCM0 shared with WT CM1, such as *Ank2*, *Fgf13*, and *Mhrt* (Fig. 6b), exhibited similar expression levels. However, other common genes among CM1, CM2, and CM3, like *Fhl2*, were downregulated in mCM0 (Supplementary Data 4), suggesting their potential transcriptional regulation by Dhx36. Furthermore, mCM0 showed higher expression of genes shared with the hypertrophic[11] non-regenerative WT CM5 cluster, including *Xirp2* and *Enah* (Fig. 6b and Supplementary Data 4). Overall, mCM0 represents a non-regenerative, stressed population of cardiomyocytes with limited proliferation or regenerative capacity, emerging post-injury or, in our case, after *Dhx36* deletion.

To comprehensively characterize Dhx36-dependent transcriptional changes, we identified differentially expressed genes between WT and mutant cardiomyocytes (Supplementary Data 4). In these analyses, several genes were observed to be upregulated in KO hearts, including *Xirp2*, *Kcnh7*, *Hcn1*, *Fmn1*, *Bcl2*, *Acta1*, *Nppa*, *Tpm2*, and *Prune2*. Some, like *Xirp2*, *Nppa*, and *Acta1*, may be linked to injury-induced responses, while others, such as *Nkx2-5*, could potentially be stabilized at the RNA level in a Dhx36-dependent manner, as previously shown[8]. In mutant mice, Dhx36 also regulated *Nkx2-5* mRNA translation, leading to a concurrent reduction in the Nkx2-5 protein levels in PD7 mutant hearts (Supplementary Fig. 8a).

While acknowledging the need for additional research to clarify the roles of upregulated genes in KO hearts, we mainly focused on the study of downregulated genes in KO hearts, particularly those with G4 structures in their promoters, as prime candidates for transcriptional regulation by Dhx36.
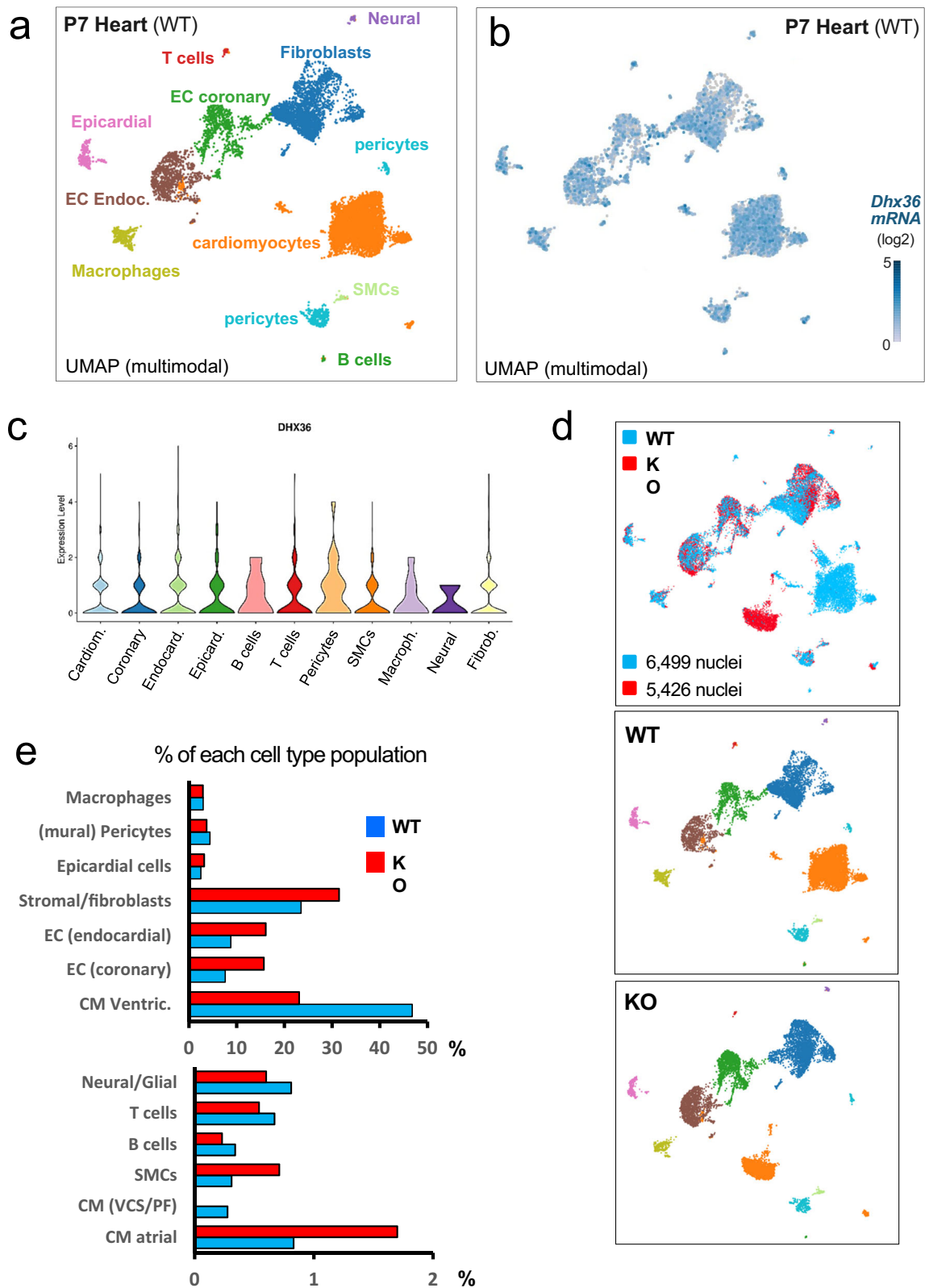
Fig. 5 | Single-nucleus RNA sequencing (snRNA-seq) and snATAC-seq multiome of neonatal WT and _Dhx36^Tnnt2_ mutant hearts. a Multimodal Uniform Manifold Approximation Projection (UMAP) visualization of cell clusters in WT hearts, randomly colored by identity. **b** Heatmap illustrating expression of _Dhx36_ in each cell cluster, projected on the UMAP graph of WT heart. **c** Violin plots presenting expression of _Dhx36_ in individual cell clusters. **d** Multimodal UMAPs displaying all WT cells in blue (_n_ = 6499) and cKO cells (_n_ = 5426) in red (upper panel). Below, WT and KO cells are separated in their multimodal UMAPs, randomly colored by identity as in (**a**). **e**, Fraction (%) of cell population clusters in each sample. Refer to Supplementary Fig. 6 for additional details. EC coronary = Coronary endothelial cells; EC Endoc.= Endocardial endothelial cells; SMCs= Smooth muscle cells.
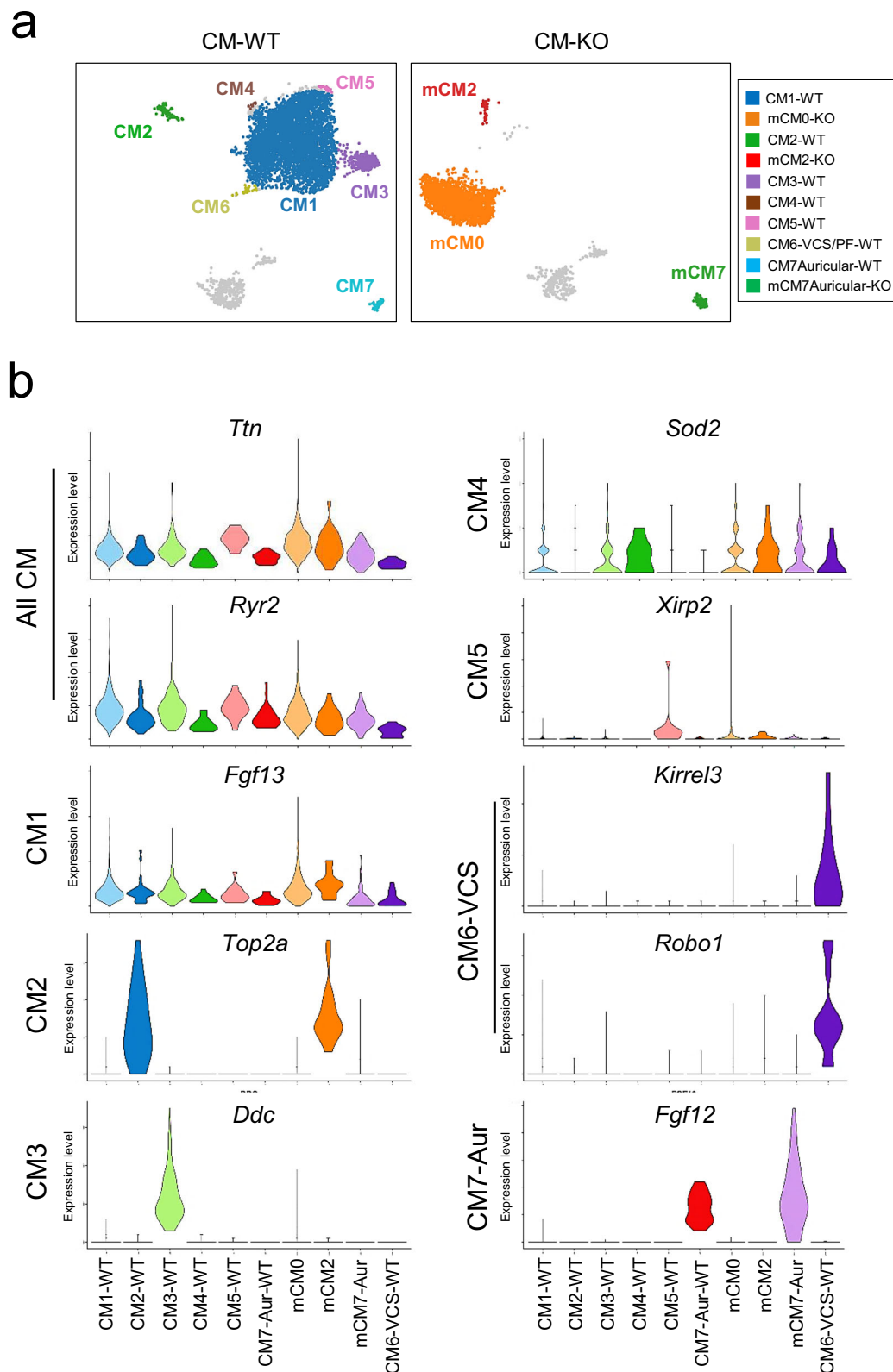
Fig. 6 | Single-nucleus RNA sequencing (snRNA-seq) and snATAC-seq multiome identify differences between WT and mutant hearts in cardiomyocyte populations. a Zoomed UMAP visualization of cardiomyocyte clusters colored by identity in the WT (left) and the mutant heart (right). **b** Violin plots depicting the expression of specific representative genes for each cardiomyocyte subcluster. Refer to Results for definition of CM clusters.

Dhx36 regulates cell type-specific gene regulatory networks in cardiomyocytes

To explore the impact of Dhx36 on cardiomyocyte gene regulatory networks, we conducted a differentially accessible (DA) test comparing KO and WT cardiomyocytes. Analysis of ATAC-seq data identified 679 DA chromatin regions in KO cardiomyocytes compared to WT (Supplementary Data 5). The intersection of differentially expressed genes (DEG) and genes associated with these DA regions

revealed 58 downregulated genes (34% of 181) in KO cardiomyocytes, including key transcription factors like *Gata6, Fosl2, Ppargc1a, Nr4a1*, and *Nr4a3*, as well as other pivotal genes for heart development and homeostasis, such as *Hcn4, Ntn1, Bcl2l11, Fhl2, Plekhh1*, and *Irs2* (Supplementary Data 6). RT-qPCR of PD7 hearts validated these findings (Fig. 7a), emphasizing the role of Dhx36 in cardiomyocyte transcriptional regulation.

We identified 25 enriched motifs specific to cardiomyocytes, including the Nkx family members Creb1 and Mef2a (Supplementary Data 7). ChromVAR[35] analysis revealed 206 motifs with differentially active scores, with CTCF being the most enriched in KO cardiomyocytes (Fig. 7b and Supplementary Data 7). Conversely, most motifs with differential activity scores were underrepresented in KO cardiomyocytes, including those associated with the NFY family (Nfya–c), and other transcription factors, such as Fosl2, Mef2, Tfeb/Tfe3, Nkx2-3, and Nkx2–8 (Supplementary Data 7). The intersection of enriched motifs and motifs with differential activity scores revealed 11 motifs, all less represented in KO cardiomyocytes. These motifs represent DNA binding sites for key transcription factors, like Nfya,b, Mef2a–d, Nkx2-3, 2–8, Atf1, Jun::JunB, and Creb1 (Supplementary Fig. 8b).

Dhx36-mediated regulation of G-quadruplexes in cardiomyocyte genes

To investigate the role of Dhx36 in resolving G4s in gene promoters, we examined 679 differential accessible peaks (DAP) and identified 173 that contained predicted G4s (Supplementary Data 8). G4 enrichment analysis revealed a significant association with DAPs (1.32-fold; *p*-value = 4×10^{-5}) between WT and KO cardiomyocytes (Supplementary Data 9; the sequences of G4s overlapping DAPs, and the DAPs linked to genes with overlapping G4s, are given in Supplementary Data 9).

To analyze snATAC-seq and snRNA-seq data for key downregulated genes in KO cardiomyocytes, we used coverage plots to depict Tn5 insertion events in various cardiomyocyte types (Fig. 8). DEGs were categorized into five groups (Supplementary Data 10). Groups 1 and 2 comprised downregulated genes with or without G4s in the gene body, respectively, and with or without G4s overlapping any DAP. Remarkably, group 1 included genes crucial for heart development and homeostasis, likely regulated by Dhx36, with G4s overlapping DAPs (Fig. 8a, Supplementary Fig. 9, and Supplementary Data 10). Group 2 consisted of genes with G4 regions in the gene body but lacking G4 overlap with DAPs (Fig. 8b and Supplementary Fig. 10a). Groups 3 and 4 mirrored the patterns of groups 1 and 2 but with upregulated genes (Fig. 8c and Supplementary Fig. 10b). Group 5 comprised upregulated genes in KO cardiomyocytes associated with G4s but lacking DAPs, possibly representing a gene cluster expressed in stressed cardiomyocytes in the mCM0 population (Supplementary Fig. 10c and Supplementary Data 10).

In the context of the VCS/PF network, probing Dhx36´s direct transcriptional regulation in this cluster was challenging due to its absence in KO cardiomyocytes. To address this, we conducted a bioinformatics analysis to identify G4s in key genes expressed in these specialized cardiomyocytes: *Hcn4, Cntn2, Drd2*, and *Kcne1* (Supplementary Fig. 11). These genes play crucial roles in electrical impulse transmission within the pacemaker, with some expressed across all working cardiomyocytes, such as *Kcne1*. *Kcne1* emerged as a promising candidate for direct transcriptional regulation by Dhx36, harboring a G4 region in its promoter (Supplementary Fig. 11). Similarly, *Hcn4, Cntn2* and *Drd2*, exhibited potential G4 structures that might be implicated in their transcription (Supplementary Fig. 11 and Supplementary Data 10).

To elucidate the role of Dhx36 in gene transcription through G4 structure resolution, we cloned promoters containing G4 motifs from selected genes (*Hcn4, Cntn2, Kcne1, Drd2, Bcl2l11, Ppargc1a, Ntn1, Fhl2*, and *Nr4a1*), and the G4-lacking promoter of *Dhx36* into luciferase-

expressing plasmids. We then transfected these constructs into HeLa cells, in which G4 resolution is exclusively conducted by Dhx36[3,36]. Promoters of *Dhx36, Kcne1, Bcl2l11, Ppargc1a, Ntn1, Fhl2*, and *Nr4a1*, exhibited transcriptional activities, with *Dhx36* and *Bcl2l11* promoters showing stronger activity (Fig. 9a and Supplementary Fig. 12). The CCS markers *Hcn4, Cntn2* and *Drd2*, also showed transcriptional activity (Fig. 9b). Treatment with the G4-quadruplex interactor TMPyP4[37] significantly reduced the luciferase activity in the pGL4 constructs, except for the *Dhx36* promoter (Fig. 9 and Supplementary Fig. 12).

In summary, our findings indicate that Dhx36 plays a major role in cardiomyocyte differentiation and CCS morphogenesis by influencing gene expression, chromatin accessibility, and transcriptional regulation through G4 resolution in various cardiomyocyte/cardiac populations.

Discussion

We demonstrate here that the G4 resolvase Dhx36 plays an essential role in the differentiation, development, and function of the mammalian CCS and working myocardium via a transcriptional mechanism. Using different stage-specific Cre drivers to conditionally abrogate *Dhx36* in mice (Fig. 10), we found that Dhx36 regulates several steps in cardiac development and homeostasis, with a high expression during heart development that gradually declined after birth and during adulthood. When *Dhx36* was deleted in embryonic cardiomyocytes, mutant mice survived to adulthood yet exhibited overt QRS complex and PR interval prolongation compared to WT, indicative of dilated cardiomyopathy and non-compaction/hypertrabeculation of the left ventricular myocardium. Moreover, *Dhx36^Tnnt2* mutant embryos and newborns showed impaired expression of key CCS markers and failed to develop a normal Purkinje fiber network, underscoring the role of Dhx36 in regulating CCS morphogenesis and function.

Notably, the timing of deletion of *Dhx36* is crucial. We observed a distinct phenotypic outcome when *Dhx36* was deleted just after birth: this led to formation of a VCS that was hypoplastic, with a milder electrical phenotype, while deletion during embryogenesis led to an undetectable (hypoplastic) VCS. Thus, Dhx36 appears to participate in the process of ventricular wall maturation and the generation of the Purkinje fiber network. Our results also highlight the dual roles of Dhx36 in working cardiomyocytes and specific CCS cardiomyocytes. *Dhx36* deletion in perinatal cardiomyocytes induced a dilated cardiomyopathy phenotype, with a predominant impact on the LVEF rather than causing significant cardiac electrical alterations. However, deletion of *Dhx36* in developing cardiomyocytes induced additional effects on the development and function of the CCS, manifested as both dilated cardiomyopathy and defective cardiac impulse generation and propagation. Both phenotypes carry a high-risk of thrombus formation in the atria, highlighting the underlying cardiomyopathy and risk of potential thromboembolic events.

As mentioned, we employed multiple cardiomyocyte-specific Cre drivers to assess the impact of *Dhx36* deletion in cardiomyocytes. The timing of deletion (embryonic versus postnatal/adult) and its extensive coverage across the myocardium complicated our ability to isolate cell-autonomous effects within the VCS. This challenge makes it difficult to ascertain whether the phenotypes observed in the VCS are attributable to intrinsic cardiomyocyte dysfunction or to secondary effects from neighboring cells. These limitations underscore the need for further research to delineate the specific contributions of Dhx36 to cardiac physiology and pathology.

Our multiomic snRNA-seq and ATAC-seq on *Dhx36^Tnnt2* mutant and WT hearts at PD7 revealed the intricate composition of the cardiomyocyte clusters. PD7 WT hearts had up to seven clusters, with CM1 (the predominant one) comprising fully differentiated working cardiomyocytes and CM4, cardiomyocytes that maintain proliferative and pro-survival capabilities through the NFYa and NFE2L1 transcription factors[11]. Notably, PD7 mutant hearts lacked CM4 cardiomyocytes,

a

b

Fig. 7 | Widespread transcriptomic alterations of mutant versus WT cardiomyocytes. a Quantitative PCR of selected cardiac conduction system genes and genes deregulated in the snRNA-seq between WT ($n = 3$) and mutant neonatal PD7 (KO; $n = 3$) hearts. **b** CTCF motif enriched at mutant cardiomyocyte-active open chromatin regions compared to WT (left). UMAPs of a zoom of the KO and WT cardiomyocytes, depicting their level of open chromatin at CTCF motifs (right).

Violin plots of Z scores of CTCF open chromatin in specific CM1/mCM0, CM2/mCM2 and auricular CM7/mCM7 CM-specific clusters are shown below. Inset boxplots show the median, lower and upper hinges as well as whiskers as in Fig. 2d and i. Significance was determined in **a** using unpaired two-sided t-test; the data are presented as mean ± SEM with the p-values inserted. Source data for **a** and **b** are provided in the source data file.

suggesting that Dhx36 helps to establish CM4 cells post-neonatally following injury. Indeed, *Dhx36* mutant mice lack regenerative capacity after postnatal myocardial infarction[9]. In mutant cardiomyocytes,

Fig. 8 | G4 structures and transcriptional alterations of Dhx36 gene targets.
a Examples (*Ntn1* and *Nr4a1*) of genes downregulated in KO CMs (Supplementary Data 10) with G4s overlapping open chromatin in their promoters (TRUE). **b** Example (*Esrrb*) of a gene downregulated in KO CMs with G4 not overlapping open chromatin in its promoter (FALSE). **c** Example (*Rai2*) of a gene upregulated in KO CMs with G4s overlapping open chromatin in their promoters (TRUE). On the left, the plots show the ATAC-seq data with the peaks of open chromatin in the promoter regions of the genes in all ventricular WT CMs (CM1) or mCM0, in WT + KO atrial CMs (CM7), and in VCS/PF (CM6) cardiomyocytes. The corresponding gene (with accessible peak represented as a grey box), the TRUE G4 (blue colored box) or FALSE G4 (salmon colored box) and the links between the regulatory regions (lower) are also shown. On the right, the violin plots of RNA-seq expression of the genes are shown in each cluster.

the proliferative NFYA, B, and C motifs are underrepresented in open chromatin (Supplementary Fig. 8b), suggesting that Dhx36 may be involved in the activation of this pathway following injury. In contrast, both the WT and mutant heart contained the proliferative CM2 cluster, and the atrial cardiomyocytes (CM7) subset, although the latter was present at higher levels in mutant hearts, perhaps to compensate for the massive demise of cardiomyocytes. Another compensatory mechanism could potentially be explained by the observed increase in Neuregulin-1 (*Nrg1*) expressing cardiac populations.

Strikingly, the predominant cardiomyocyte population in the mutant heart—mCM0—resembles the hypertrophic, non-regenerative CM5 cluster (which was nearly absent from our PD7 WT hearts, in line with previous findings[11]). The mCM0 population also presents a Dhx36-dependent transcriptional signature that is likewise evident in the mCM2 and mCM7 populations, suggesting a shared transcriptional response to the stress induced by *Dhx36* deletion. Intriguingly, several genes that are upregulated in the mutant clusters harbor dG4 motifs in their promoters (such as *Bcl2*, a well-established transcriptionally G4-dependent gene[38]). This is counterintuitive because it is thought that Dhx36 positively regulates transcription by resolving promoter-G4 knots. Our results might reflect a general upregulation of an anti-apoptotic factor in the stressed mutant cardiomyocytes, but it could also reflect a negative transcriptional regulation of Dhx36 on these dG4-containing promoters; further investigations are required to address this.

We also identified several genes that are downregulated in the mutant cardiomyocytes with dG4 motifs overlapping with differentially accessible (DA) peaks in their promoters, which are potentially regulated by Dhx36's dG4-resolving activity; these include *Hcn4*, *Drd2*, *Cntn2*, *Kcne1*, *Bcl2l11*, *Ppargc1a*, *Ntn1*, *Fhl2*, and *Nr4a1*. The transcriptional activity of these promoters was selectively abrogated by the G-quadruplex interactor TMPyP4. As these genes are crucial in heart physiology, we propose that their downregulation in mutant hearts may contribute to upstream electrical defects, both reliant on and independent of direct involvement in the Purkinje network. Of note, the genes *Kcnq1*/*Kcne1*, crucial for heart action potentials, are expressed in all cardiomyocytes. We hypothesize that *Kcne1* expression might be involved in functional defects of mutant hearts, rather than directly contributing to VCS morphogenesis. In turn, Netrin1 (*Ntn1*) (also downregulated in mutant hearts) is a secreted laminin-like protein that regulates axon guidance for GABAergic neurons[39] and has cardioprotective properties[40–43].

We have identified a small yet significant cluster of VCS cardiomyocytes in WT heart that are entirely absent in mutant hearts in the snRNA-seq dataset, which consist of a cluster of PF cells (CM6) expressing CCS lineage-specific genes (e.g., *Cntn2*, *Tbx3*, *Robo1*, *Cpne5*, *Sema3a*, and *Ncam1*). Our differential expression analysis comparing this WT VCS/PF cluster to the prevalent WT CM1 cluster revealed potential PF gene markers, including *Shisa9*, *Kirrel3*, *Slit2/3*, *Col4a3*, *Col4a4*, *Ephb1*, *Ntm*, and *Plxdc2* (Supplementary Data 3, 4). Moreover, gene ontology analysis implicated certain genes in this cluster (*Robo1*, *Slit2/3*, *Sema3a/c*, and *Ephb1*) in axon guidance, suggesting a potential involvement in PF network morphogenesis. For instance, the Netrin-1/DCC and Robo/Slit signaling axes regulate axon guidance through attraction/repulsion mechanisms, which may govern the positioning, migration, and morphogenesis of VCS/PF cardiomyocytes[44]. Robo/Slit signaling is particularly important in heart development, contributing to processes such as cell migration, ventricular septum formation, and valve development[44,45]. Our findings suggest that the Robo/Slit pathway may also contribute to the development and function of VCS/PF network morphogenesis. In cases of defective Robo/Slit signaling, alternative pathways may compensate. The observed upregulation of Neuregulin 1 (Nrg1) hints at a potential compensatory mechanism, although it is possible that defects in other undetermined secreted factors or cell-to-cell
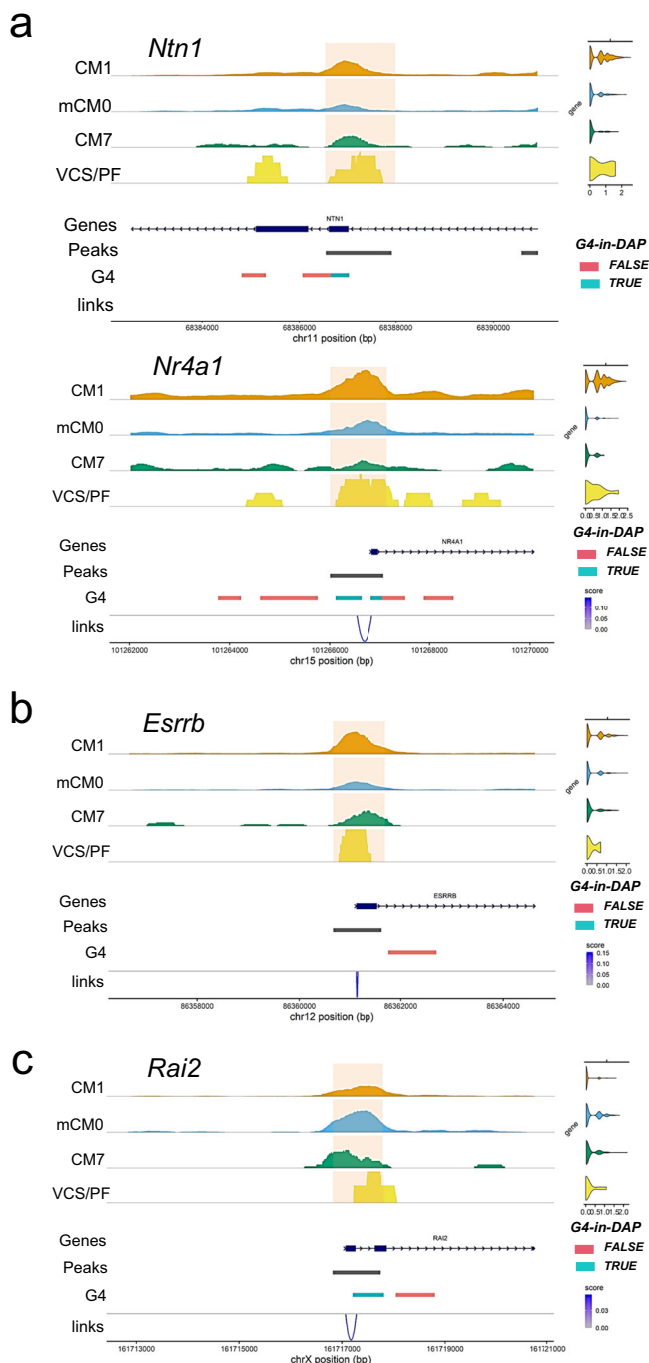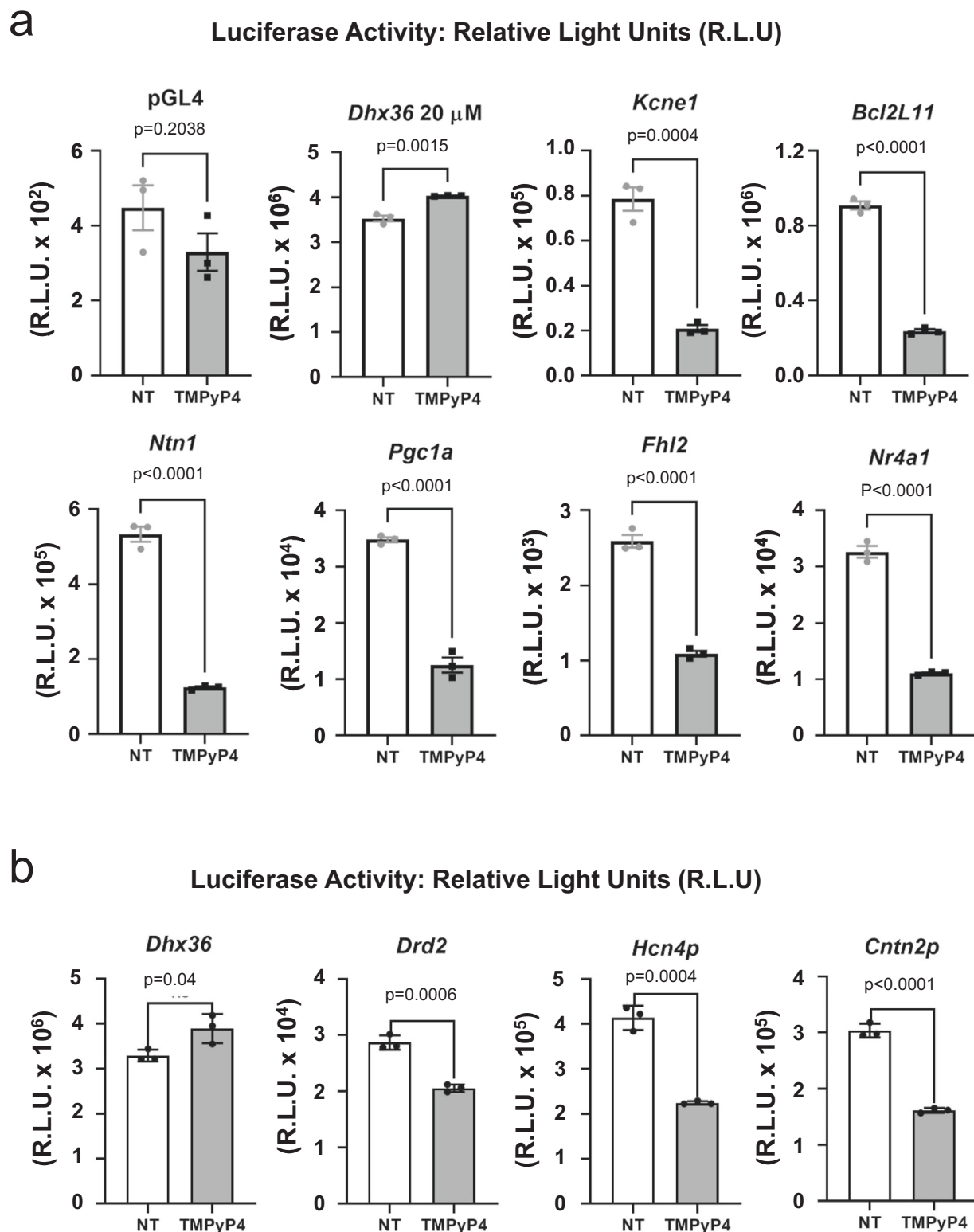
Fig. 9 | G4-resolvase-dependent transcriptional activation of Dhx36 CM target genes. a Luciferase transcriptional activation assays in HeLa cells of promoter regions of *Dhx36*, *Kcne1*, *Bcl2l11*, *Ntn1*, *Ppargc1a (Pgc1a)*, *Fhl2*, and *Nr4a1* cloned in pGL4.25 luciferase expressing vector. The luciferase activity, measured in Relative light units (R.L.U.) of the different constructs, are shown in the presence or absence of 20 μM of the G4 stabilization drug TMPyP4. **b** same as in (**a**) with *Dhx36*, *Drd2*,

Hcn4 and *Cntn2* promoters. The pGL4.25 vector, presenting a minimal promoter, is shown as a negative control. Significance was determined in **a** and **b** using unpaired two-sided *t*-test; the data with the *p*-values included are presented as mean ± SEM ($n = 3$). The experiments shown in (**a**) and (**b**) are representative of 3 independent experiments (total $n = 9$), with similar results. Source data are provided in the source data file.
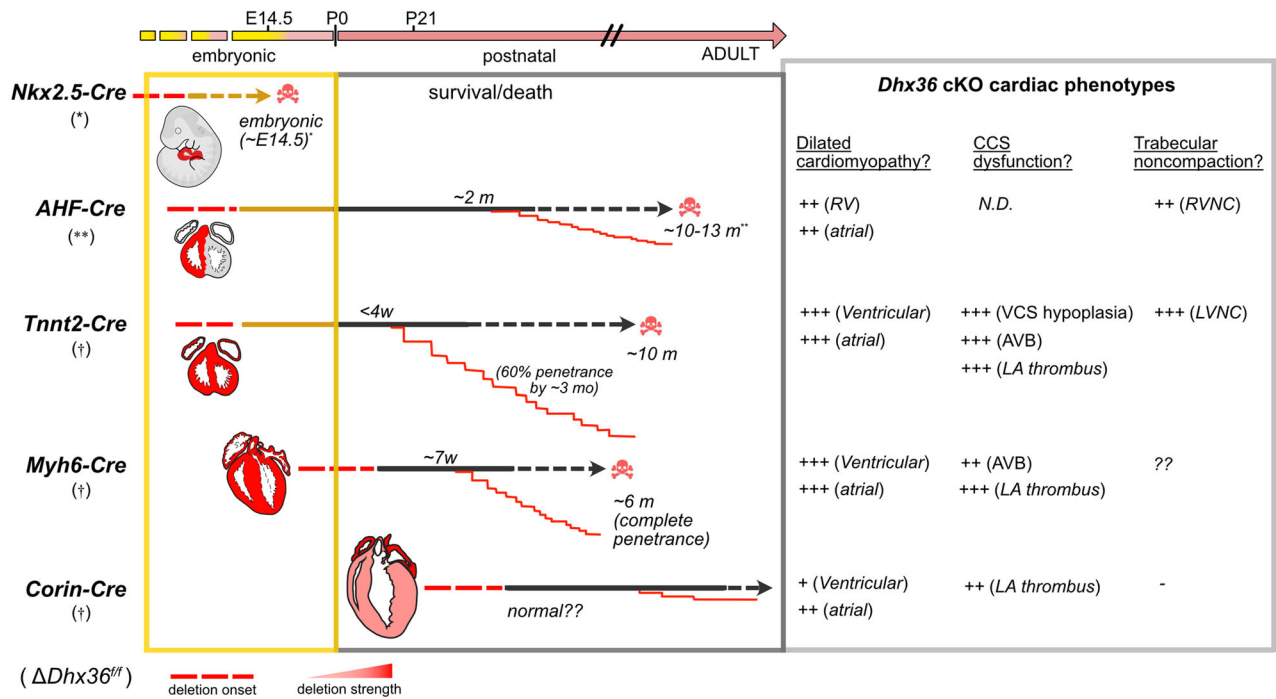
Fig. 10 | Model of the impact of *Dhx36* deletion in the heart. Cardiac phenotypes observed upon *Dhx36* deletion with the indicated *Cre*-driver lines described in this study and in Nie et al[8] and Huang et al[9]. For each mutant line, the dotted red line indicates the time window of *Cre*-driver allele action, and red shading indicates the expected anatomical recombination domain and deletion strength within the heart. Timelines depict the approximate extent of survival, the onset of lethality, and the phenotype penetrance for each driver. The panel to the right indicates the range and intensity of the cardiac phenotypes reported here and in previous studies. AVB, atrioventricular block; CCS, cardiac conduction system; LA, left atrium; LVNC, left ventricular non-compaction; RV, right ventricle; RVNC, right ventricular non-compaction; VCS, ventricular conduction system.

signaling pathways contribute to the VCS hypoplasia observed in *Dhx36^Tnnt2* mutant hearts (Fig. 4, Supplementary Fig. 2).

Another cluster entirely absent from the mutant hearts is the *dopa-decarboxylase* (*Ddc*) expressing cluster, or CM3. The Ddc enzyme converts dopa to dopamine, a signal crucial for enhancing contractile force, elevating beating rate, and constricting coronary arteries in the heart[46]. *Ddc* is a determinant gene in right ventricle maturation[47] and is potentially involved in later stages of VCS morphogenesis, perhaps interconnected with the Netrin-1 signaling pathway, which is also involved in dopaminergic neurons[39]. *Ddc* is one of approximately 200 imprinted genes whose expression is regulated paternally or maternally through DNA methylation[47]. *Ddc* expression appears to be regulated via a CTCF-dependent insulator of the neighboring gene *Grb10*[48] and a *Ddc* intronic CTCF site (intron 12) that interacts with the *Grb10* intronic CTCF regions and CTCF-dependent insulator regions. Remarkably, our data show a G-quadruplex motif with G-score of 63[49–53] near the CTCF binding site in *Ddc*'s intron 12 (Supplementary Data 9). We hypothesize that resolving this G4 may influence the 3D structure around the insulator, thereby impacting *Ddc* transcription. Furthermore, this CTCF stands out as the most enriched motif in mutant vs. WT cardiomyocytes (Fig. 7b). We postulate that this transcriptional downregulation of *Ddc* may explain the absence of the CM3 population in mutant hearts, and its impact on VCS morphogenesis via the disruption of the secretable Netrin/dopamine signaling.

Dhx36 modulates *Nkx2-5* mRNA at both the posttranscriptional and translational levels[8]. Indeed, in *Dhx36* KO hearts, *Nkx2-5* mRNA levels were increased, while protein levels were reduced in PD7 mutant hearts. Nkx2-5 haploinsufficiency results in ventricular conduction system and Purkinje fibers hypoplasia and conduction defects in mice[54,55]. We though hypothesize that reduced Nkx2-5 protein alone does not fully account for the PF network hypoplasia observed in mutant hearts. For instance, we also observed reductions in other key cardiac targets, including *Ntn1, Nur77, and Pgc1a*, which are not directly regulated by Nkx2-5 but exhibited distinct Dhx36-dependent transcriptional downregulation patterns in mutant hearts. Moreover, the downregulation of *Hcn4* is unlikely to be due to reduced Nkx2-5 levels, as Nkx2-5 has been reported to negatively regulate *Hcn4* gene expression[56].

Our study provides insights into the complex roles of Dhx36 in cardiomyocyte differentiation and CCS morphogenesis, identifying crucial genes and pathways that regulate the development and function of the VCS/PF network. Future research should focus on elucidating the specific roles of the newly identified targets, as well as the role of Dhx36 in transcriptional regulation, chromatin accessibility, and G4 resolution during these processes. Our findings in mice cannot be directly extrapolated to human pathology. In fact, to date, no mutations in DHX36 have been associated with human heart disease. However, it may be challenging to identify non-lethal mutations in DHX36, given the gene's critical role in early development, as evidenced by the fact that complete *Dhx36* knockout in mice results in implantation failure. A crucial direction for future research will be to identify DHX36 mutations that contribute to cardiovascular diseases. These endeavors address not only fundamental questions about heart physiology but could also potentially guide the development of therapeutic strategies for heart conditions.

Methods
Mice, embryos, and genotyping
The *Dhx36^floxed* mouse strain has been described previously[6] and was kindly provided by Dr. Nagamine. Transgenic Cre mouse lines, including *MCK^Cre/wt*, *Nkx2.5^Cre/wt*, *Tnnt2^Cre/wt*, and *Myh6^Cre/wt*, were employed previously[25,28,29,57]. The Connexin 40 GFP line (*Cx40-eGFP*),

characterized by the insertion of the green fluorescent protein cDNA into the connexin 40 (*Gja5*) locus, allowing for the visualization of CCS architecture, was kindly provided by Dr. Miquerol[31]. All animals used in this study were in a C57bl/6-CD1 mixed background. Sex was not considered in the study design and analysis, because we did not find phenotypic differences between males and females. Animal welfare adhered to the guidelines and conformed to EU Directive 2010/63EU and Recommendation 2007/526/EC, enforced by Spanish law under Real Decreto 53/2013. All experiments involving mice and embryos were approved by the CNIC Animal Experimentation Ethics Committee and licensed by the relevant authorities in the Madrid Region (PROEX 346/15).

Promoter cloning and luciferase assay

The promoters or G4-containing regions of the tested genes were obtained through conventional PCR, using mouse genomic DNA (primer sequences listed in Supplementary Data 11). Purified PCR products were cloned into the XhoI-linearized pGL3-Basic vector using the recombination-based NEBuilder HiFi DNA assembly master mix, following the manufacturer´s recommendations (New England Biolabs; #E2621L). Subsequently, the cloned DNA fragments within pGL3-Basic were excised with SacI and BglII and then directionally inserted into pGL4.25 (Addgene #E8431), a vector featuring a minimal promoter and expressing a highly unstable luciferase protein.

For transfection, 40,000 HeLa cells per well were seeded in 24 well plates and transfected with 0.5 µg of pGL3 or pGL4.25 constructs using the Lipofectamine 3000 transfection Reagent (ThermoFisher Scientific # L3000008), following manufacturer´s recommendations. After 24 h, cells were treated with or without 20 µM of the the G4 stabilizer TMPyP4 (MedChemExpress #HY-108477) for an additional 24 h. Luciferase activity was then measured using a Sirius Luminometer (Berthold) for 30 s. The experiments were conducted in triplicate and repeated at least three times ($n = 9$).

Single-nucleus ATAC + RNA-seq multiome experiment and bioinformatics analysis

Whole hearts from 7-day-old PD7 wild-type (WT) (*Dhx36^{f/f};Tnnt2^{wt/wt}*) and mutant (*Dhx36^{f/f};Tnnt2^{cre/wt}*) mice were dissected, chopped into several pieces, snap-frozen and stored in liquid nitrogen. On the day of the experiment, wild-type and mutant hearts were pooled (two each), and nuclei were isolated using the Chromium Nuclei Isolation Kit with RNAse inhibitor (10X Genomics; #PN-1000494) following the manufacturer's recommendations. Nuclei were captured in the Chromium Controller (10X Genomics) and processed with the Chromium Next GEM single cell Multiome ATAC+Gene Expression (GEX) Kit (10X Genomics; #PN-1000285). This kit enables simultaneous profiling of chromatin accessibility and gene expression in the same single nuclei, generating ATAC and GEX libraries from the same pool of pre-amplified Tn5 transposed DNA/cDNA. Bulk sequencing was performed on the Illumina NextSeq 2000, with Cell Ranger v8.0 from 10X Genomics used for de-multiplexing and mapping to the mouse genome GRCm38/10 under default parameters. Median values for wild type included 4305 UMIs per cell (1976 median genes per cell) and 6434 high-quality ATAC fragments per cell. For KO, median values were 5180 UMIs per cell (2394 median genes per cell) and 5748 high-quality ATAC fragments per cell (Supplementary Fig. 5b)

Bioinformatics analysis was conducted in R using Seurat v4[58] and Signac v10[59] packages. RNA and ATAC assays underwent independent pre-processing with basic QC, filtering cells based on detected molecules for each modality (between 2000 and 30,000), detected genes or peaks (>800), as well as mitochondrial percentage (<20%). We used SCTransform for RNA data normalization, and PCA dimensionality reduction, and used 50 PCs to generate RNA-based Uniform Manifold Approximation and Projection (UMAP) representations. Latent semantic indexing (LSI) was employed for ATAC data, which performs

term frequency-inverse document frequency (TF-IDF) normalization, and singular value decomposition (SVD) to reduce the dimensionality. The initial 50 LSI components, excluding the first one that codifies technical (information about sequencing depth) and not biological variation were used to construct ATAC-based UMAP representations. Integration of information from both single-cell modalities was performed through weighted nearest neighbor analysis (WNN) that generates a graph codifying closest neighbors based on a cell-specific weighted combination of RNA and ATAC using the previously selected PCA and LSI components, respectively. The final multimodal non-linear dimensionality reduction (UMAP) and clustering (Louvain algorithm with resolution 0.2) were constructed from the multimodal WNN graph generated before. Next, data were manually inspected and analyzed using Loupe Browser, for further filtering and detailed refinement of clustering results to obtain a final labelling of cell populations.

Further analyses were performed from the final clean and labelled dataset. For each gene, we found the set of peaks that may regulate the gene (linked peaks) by computing the correlation between gene expression and accessibility at nearby peaks, and correcting for bias due to GC content, overall accessibility, and peak size. Next, we performed contrasts between WT and KO cardiomyocytes at gene expression and ATAC peak levels. To find differentially accessible regions between those clusters of cells, we performed a differential accessibility (DA) test using logistic regression and added the total number of fragments as a latent variable to mitigate the effects of differential sequencing depth on the result. To run gene differential expression (DE), we used corrected counts (obtained by setting the sequencing depth for all the cells to a fixed value and reversing the learned regularized negative-binomial regression model), and then performed differential expression using Wilcoxon test. Intersections of DE genes and genes linked to DA peaks were also reported. *P*-value adjustments were performed using the Bonferroni correction, and average log2 fold changes were reported.

Motif analysis was performed using DNA sequence motif information from JASPAR database. To identify potentially important cell type-specific regulatory sequences, we searched for motifs that are overrepresented (enriched motifs) in the set of peaks that are differentially accessible between cell types. We performed a hypergeometric test to get the probability of observing the motif at the given frequency by chance, as compared to a background set of peaks matched for GC content. Concurrently, motif activities were generated using chromVAR[35], computing a per-cell score that allow the visualization of motif activities per cell and provide an alternative method of identifying differentially active motifs between cell types.

G4 analysis was performed using GAIA database[53] with G4 predictions of mouse generated by G4RNA screener[49–52]. We computed the existence (or not) of predicted G4s overlapping each peak region. Then, we analyzed whether G4s are enriched/overrepresented in chromatin sites with DA. We performed a hypergeometric test to test the probability of having G4s in DA peaks at the given frequency by chance, comparing with a background set of peaks matched for GC content and sequence length.

Most of the data from sn-multiome have been extracted in the Supplementary Data 2 to 9. For raw data availability, check the Data Availability Statement.

Histological analysis

Embryo and adult hearts were fixed overnight in 4% paraformaldehyde (vol/vol) in PBS, following by paraffin embedding and microtome sectioning for hematoxylin and eosin (H&E) staining using standard procedures. In situ Hybridization, Immunohistochemistry (IHC) and immunofluorescence (IF) were conducted using standard procedures.

For whole-mount IF, adult hearts incised along the inter-ventricular septum, pinned in siliconized petri dishes to expose the left

ventricles, and fixed for 2 h with 4% paraformaldehyde. After extensive PBS washing, permeabilization with 0.5% Triton X100 in PBS, and blocking with PBS containing 3% BSA and 0.1% Triton-X 100, samples were incubated with primary antibody and fluorescent-coupled secondary antibodies in blocking buffer. The stained samples were observed under a scope and a confocal microscope[31].

Echocardiography and electrocardiography (ECG)

Echocardiography and ECG recordings were obtained as previously described[60]. Briefly, mice were anesthetized through inhalation of isoflurane (0.5–1.25%) and oxygen (98.75%). For ultrasound studies, a 30 MHz transthoracic echocardiography probe was employed, and images were captured using Vevo 2100 (VisualSonics, Toronto, Canada). The acquired images underwent blind analysis by skilled operators from CNIC advanced imaging unit, using the Vevo 2100 Workstation software.

ECG tracings were recorded from sedated animals, as detailed elsewhere[61]. Briefly, ECG recordings were acquired for 60 s at 2 KHz sweep-speed using a MP36R data acquisition workstation (Biopac Systems). Data were stored for offline analysis using custom MatLab scripts for pre-processing, visualization and quantification of electrophysiological intervals and heart rate[62]. Lead II was chosen for analysis. Following QRS complex, P and T wave detection, ECG intervals were extracted using adaptive windowing based on beat-to-beat R-R changes. PR intervals were measured from the onset of the P wave to the start of the R wave/Q wave, and QRS intervals from the beginning of the Q wave to where the S wave intersects the baseline. QRS amplitude was measured peak-to-peak from the maximum positive deflection to the minimum negative deflection on the QRS complex. A sub-domain of normal RR variability (percentile 100th) was established from ECG traces of wild-type mice. Sinus node dysfunction was defined when the mouse specific RRn+1 vs RRn domain partially or completely deviated from the normal RR variability sub-domain identified in controls. Additionally, dimensionless R-R intervals were plotted over the 60 s electrocardiogram recordings to detect alterations in sinus rhythm.

RNA sequencing and statistical analysis

For transcriptional profiling of adult organs, whole hearts (including atria) were surgically isolated from 2- to 3-week-old WT or *Dhx36^myh6* mice. The isolated organs were individually submerged into 1 mL TRIsure buffer (Meridian Bioscience #BIO-38032), immediately snap-frozen in liquid N_2, and stored at −80 °C. Tissue homogenization was performed using the MagNA lyser system (Roche), and total RNA was isolated. RNA from 5–6 hearts per genotype was pooled and purified on Qiagen-RNA-clean columns (Qiagen #74204). Experiments were conducted in triplicate (3 WT and 3 mutant pools). RNA sequencing procedures were previously described[60].

Numerical data are presented as mean ± SEM. Differences between WT and mutant groups were statistically assessed using unpaired two-tailed Student´s t-test for most experiments or χ^2 in Kaplan-Meier survival curves. Statistical significance was considered at $p < 0.05$.

The data from RNA-seq have been extracted in the Supplementary Data 2. The raw data has been deposited (refer to Data availability section).

qPCR analysis

Quantitative real-time PCR (qPCR) of genes of interest and housekeeping genes was performed on the same RNA-pooled samples used for RNA-seq experiments. SYBR Green PCR master mix (Applied BioSystems) was used for qPCR analysis. Total RNA from neonatal PD0-PD1 or PD7 hearts was extracted and pooled as described in the corresponding Figure Legends, and indicated qPCRs were performed. The primer sequences used for qPCR and promoter cloning are provided in

Supplementary Data 11. Statistically significance was assessed using unpaired two-tailed Student´s t-test.

Protein analysis

Western blotting was used to detect the presence of Dhx36 protein in the cytoplasm and nuclei of whole hearts (Fig. 1c), as well as Dhx36 and Nkx2-5 in whole extracts from WT and *Dhx36^Tnnt2* PD7 hearts (Supplementary Fig. 8a). Tubulin was used as a loading control in the same gel where Dhx36 was detected (Fig. 1c). Similarly, in Supplementary Fig. 8a, PSF was used as a loading control in the same gel where Nkx2-5 was detected. Uncropped and unprocessed scans of the blots are available in the Source Data file for Fig. 1c, and in the Supplementary information file for Supplementary Fig. 8a.

Reporting summary

Further information on research design is available in the Nature Portfolio Reporting Summary linked to this article.

Data availability

Source data are provided with this paper in the Source data file. Most of the data that support the findings of this study are extracted in the Supplementary Data 2–9. All raw data have been deposited in the EMBL´s European Bioinformatics Institute (https://www.ebi.ac.uk). Raw data for bulk RNA-seq have been deposited with code E-MTAB-14440. The snATAC-seq and snRNA-seq raw data have been deposited with codes E-MTAB-14441 and E-MTAB-14442, respectively.

References

1. van Eif, V. W. W., Devalla, H. D., Boink, G. J. J. & Christoffels, V. M. Transcriptional regulation of the cardiac conduction system. *Nat. Rev. Cardiol.* **15**, 617–630 (2018).
2. Antcliff, A., McCullough, L. D. & Tsvetkov, A. S. G-Quadruplexes and the DNA/RNA helicase DHX36 in health, disease, and aging. *Aging (Albany NY)* **13**, 25578–25587 (2021).
3. Creacy, S. D. et al. G4 resolvase 1 binds both DNA and RNA tetramolecular quadruplex with high affinity and is the major source of tetramolecular quadruplex G4-DNA and G4-RNA resolving activity in HeLa cell lysates. *J. Biol. Chem.* **283**, 34626–34634 (2008).
4. Giri, B. et al. G4 resolvase 1 tightly binds and unwinds unimolecular G4-DNA. *Nucleic Acids Res.* **39**, 7161–7178 (2011).
5. Tran, H., Schilling, M., Wirbelauer, C., Hess, D. & Nagamine, Y. Facilitation of mRNA deadenylation and decay by the exosome-bound, DExH protein RHAU. *Mol. Cell* **13**, 101–111 (2004).
6. Lai, J. C. et al. The DEAH-box helicase RHAU is an essential gene and critical for mouse hematopoiesis. *Blood* **119**, 4291–4300 (2012).
7. Sauer, M. et al. DHX36 prevents the accumulation of translationally inactive mRNAs with G4-structures in untranslated regions. *Nat. Commun.* **10**, 2421 (2019).
8. Nie, J. et al. Post-transcriptional Regulation of Nkx2-5 by RHAU in Heart Development. *Cell Rep.* **13**, 723–732 (2015).
9. Huang, X. et al. The G4 resolvase RHAU regulates ventricular trabeculation and compaction through transcriptional and posttranscriptional mechanisms. *J. Biol. Chem.* **298**, 101449 (2022).
10. Jiang, M. et al. The G4 resolvase RHAU modulates mRNA translation and stability to sustain postnatal heart function and regeneration. *J. Biol. Chem.* **296**, 100080 (2021).
11. Cui, M. et al. Dynamic Transcriptional Responses to Injury of Regenerative and Non-regenerative Cardiomyocytes Revealed by Single-Nucleus RNA Sequencing. *Dev. Cell* **53**, 102–116 e108 (2020).
12. Wang, Z. et al. Cell-Type-Specific Gene Regulatory Networks Underlying Murine Neonatal Heart Regeneration at Single-Cell Resolution. *Cell Rep.* **33**, 108472 (2020).
13. Chaffin, M. et al. Single-nucleus profiling of human dilated and hypertrophic cardiomyopathy. *Nature* **608**, 174–180 (2022).

14. Elorbany, R. et al. Single-cell sequencing reveals lineage-specific dynamic genetic regulation of gene expression during human cardiomyocyte differentiation. *PLoS Genet* **18**, e1009666 (2022).

15. Feng, W. et al. Single-cell transcriptomic analysis identifies murine heart molecular features at embryonic and neonatal stages. *Nat. Commun.* **13**, 7960 (2022).

16. Jia, G. et al. Single cell RNA-seq and ATAC-seq analysis of cardiac progenitor cell transition states and lineage settlement. *Nat. Commun.* **9**, 4877 (2018).

17. Koenig, A. L. et al. Single-cell transcriptomics reveals cell-type-specific diversification in human heart failure. *Nat. Cardiovasc Res.* **1**, 263–280 (2022).

18. Litvinukova, M. et al. Cells of the adult human heart. *Nature* **588**, 466–472 (2020).

19. Tucker, N. R. et al. Transcriptional and Cellular Diversity of the Human Heart. *Circulation* **142**, 466–482 (2020).

20. Fan, W., Yang, C., Hou, X., Wan, J. & Liao, B. Novel Insights into the Sinoatrial Node in Single-Cell RNA Sequencing: From Developmental Biology to Physiological Function. *J. Cardiovasc. Dev. Dis.* **9**, 402 (2022).

21. Goodyer, W. R. et al. Transcriptomic Profiling of the Developing Cardiac Conduction System at Single-Cell Resolution. *Circ. Res.* **125**, 379–397 (2019).

22. Kanemaru, K. et al. Spatially resolved multiomics of human cardiac niches. *Nature* **619**, 801–810 (2023).

23. Liang, D. et al. Cellular and molecular landscape of mammalian sinoatrial node revealed by single-cell RNA sequencing. *Nat. Commun.* **12**, 287 (2021).

24. Wiesinger, A. et al. A single cell transcriptional roadmap of human pacemaker cell differentiation. *Elife* **11**, e76781 (2022).

25. Bruning, J. C. et al. A muscle-specific insulin receptor knockout exhibits features of the metabolic syndrome of NIDDM without altering glucose tolerance. *Mol. Cell* **2**, 559–569 (1998).

26. Li, S. et al. Requirement for serum response factor for skeletal muscle growth and maturation revealed by tissue-specific gene deletion in mice. *Proc. Natl. Acad. Sci. USA* **102**, 1082–1087 (2005).

27. Chen, X. et al. Translational control by DHX36 binding to 5'UTR G-quadruplex is essential for muscle stem-cell regenerative functions. *Nat. Commun.* **12**, 5043 (2021).

28. Jiao, K. et al. An essential role of Bmp4 in the atrioventricular septation of the mouse heart. *Genes Dev.* **17**, 2362–2367 (2003).

29. Agah, R. et al. Gene recombination in postmitotic cells. Targeted expression of Cre recombinase provokes cardiac-restricted, site-specific rearrangement in adult ventricular muscle in vivo. *J. Clin. Invest* **100**, 169–179 (1997).

30. Cerrone, M. et al. Arrhythmogenic mechanisms in a mouse model of catecholaminergic polymorphic ventricular tachycardia. *Circ. Res* **101**, 1039–1048 (2007).

31. Miquerol, L. et al. Resolving cell lineage contributions to the ventricular conduction system with a Cx40-GFP allele: a dual contribution of the first and second heart fields. *Dev. Dyn.* **242**, 665–677 (2013).

32. Chen, E. Y. et al. Enrichr: interactive and collaborative HTML5 gene list enrichment analysis tool. *BMC Bioinforma.* **14**, 128 (2013).

33. Dennis, G., Jr., et al. DAVID: Database for Annotation, Visualization, and Integrated Discovery. *Genome Biol.* **4**, P3 (2003).

34. Sherman, B. T. et al. DAVID: a web server for functional enrichment analysis and functional annotation of gene lists (2021 update). *Nucleic Acids Res.* **50**, W216–W221 (2022).

35. Schep, A. N., Wu, B., Buenrostro, J. D. & Greenleaf, W. J. chromVAR: inferring transcription-factor-associated accessibility from single-cell epigenomic data. *Nat. Methods* **14**, 975–978 (2017).

36. Vaughn, J. P. et al. The DEXH protein product of the DHX36 gene is the major source of tetramolecular quadruplex G4-DNA resolving activity in HeLa cell lysates. *J. Biol. Chem.* **280**, 38117–38120 (2005).

37. Kim, M. Y., Gleason-Guzman, M., Izbicka, E., Nishioka, D. & Hurley, L. H. The different biological effects of telomestatin and TMPyP4 can be attributed to their selectivity for interaction with intramolecular or intermolecular G-quadruplex structures. *Cancer Res.* **63**, 3247–3256 (2003).

38. Pandya, N., Rani, R., Kumar, V. & Kumar, A. Discovery of a potent Guanidine derivative that selectively binds and stabilizes the human BCL-2 G-quadruplex DNA and downregulates the transcription. *Gene* **851**, 146975 (2023).

39. Brignani, S. et al. Remotely Produced and Axon-Derived Netrin-1 Instructs GABAergic Neuron Migration and Dopaminergic Substantia Nigra Development. *Neuron* **107**, 684–702 e689 (2020).

40. Layne, K., Ferro, A. & Passacquale, G. Netrin-1 as a novel therapeutic target in cardiovascular disease: to activate or inhibit? *Cardiovasc Res.* **107**, 410–419 (2015).

41. Li, Q. & Cai, H. Induction of cardioprotection by small netrin-1-derived peptides. *Am. J. Physiol. Cell Physiol.* **309**, C100–C106 (2015).

42. Wang, N., Cao, Y. & Zhu, Y. Netrin-1 prevents the development of cardiac hypertrophy and heart failure. *Mol. Med Rep.* **13**, 2175–2181 (2016).

43. Zhang, J. & Cai, H. Netrin-1 prevents ischemia/reperfusion-induced myocardial infarction via a DCC/ERK1/2/eNOS s1177/NO/DCC feed-forward mechanism. *J. Mol. Cell Cardiol.* **48**, 1060–1070 (2010).

44. Zhao, J. & Mommersteeg, M. T. M. Slit-Robo signalling in heart development. *Cardiovasc Res.* **114**, 794–804 (2018).

45. Zhao, J., Bruche, S., Potts, H. G., Davies, B. & Mommersteeg, M. T. M. Tissue-Specific Roles for the Slit-Robo Pathway During Heart, Caval Vein, and Diaphragm Development. *J. Am. Heart Assoc.* **11**, e023348 (2022).

46. Neumann, J., Hofmann, B., Dhein, S. & Gergs, U. Role of Dopamine in the Heart in Health and Disease. *Int J. Mol. Sci.* **24**, 5042 (2023).

47. Prickett, A. R. et al. Imprinted Gene Expression and Function of the Dopa Decarboxylase Gene in the Developing Heart. *Front Cell Dev. Biol.* **9**, 676543 (2021).

48. Juan, A. M. et al. Tissue-specific Grb10/Ddc insulator drives allelic architecture for cardiac development. *Mol. Cell* **82**, 3613–3631 e3617 (2022).

49. Beaudoin, J. D., Jodoin, R. & Perreault, J. P. New scoring system to identify RNA G-quadruplex folding. *Nucleic Acids Res.* **42**, 1209–1223 (2014).

50. Bedrat, A., Lacroix, L. & Mergny, J. L. Re-evaluation of G-quadruplex propensity with G4Hunter. *Nucleic Acids Res.* **44**, 1746–1759 (2016).

51. Garant, J. M., Perreault, J. P. & Scott, M. S. Motif independent identification of potential RNA G-quadruplexes by G4RNA screener. *Bioinformatics* **33**, 3532–3537 (2017).

52. Garant, J. M., Perreault, J. P. & Scott, M. S. G4RNA screener web server: User focused interface for RNA G-quadruplex prediction. *Biochimie* **151**, 115–118 (2018).

53. Vannutelli, A., Perreault, J. P. & Ouangraoua, A. G-quadruplex occurrence and conservation: more than just a question of guanine-cytosine content. *NAR Genom. Bioinform* **4**, lqac010 (2022).

54. Cambier, L., Plate, M., Sucov, H. M. & Pashmforoush, M. Nkx2-5 regulates cardiac growth through modulation of Wnt signaling by R-spondin3. *Development* **141**, 2959–2971 (2014).

55. Jay, P. Y. et al. Nkx2-5 mutation causes anatomic hypoplasia of the cardiac conduction system. *J. Clin. Invest.* **113**, 1130–1137 (2004).

56. Chen, J. et al. Nkx2.5 insufficiency leads to atrial electrical remodeling through Wnt signaling in HL-1 cells. *Exp. Ther. Med.* **18**, 4631–4636 (2019).

57. Stanley, E. G. et al. Efficient Cre-mediated deletion in cardiac progenitor cells conferred by a 3'UTR-ires-Cre allele of the homeobox gene Nkx2-5. *Int. J. Dev. Biol.* **46**, 431–439 (2002).

58. Hao, Y. et al. Integrated analysis of multimodal single-cell data. *Cell* **184**, 3573–3587 e3529 (2021).

59. Stuart, T., Srivastava, A., Madad, S., Lareau, C. A. & Satija, R. Single-cell chromatin state analysis with Signac. *Nat. Methods* **18**, 1333–1341 (2021).

60. Gomez-Del Arco, P. et al. The Chromatin Remodeling Complex Chd4/NuRD Controls Striated Muscle Identity and Metabolic Homeostasis. *Cell Metab.* **23**, 881–892 (2016).

61. Rivera-Torres, J. et al. Cardiac electrical defects in progeroid mice and Hutchinson-Gilford progeria syndrome patients with nuclear lamina alterations. *Proc. Natl Acad. Sci. USA* **113**, E7250–E7259 (2016).

62. Filgueiras-Rama, D. et al. Human influenza A virus causes myocardial and cardiac-specific conduction system infections associated with early inflammation and premature death. *Cardiovasc Res.* **117**, 876–889 (2021).

Author contributions

P.G-A.: Conceptualization; formal analysis; funding acquisition; project administration; resources; investigation; validation; supervision; visualization; writing – original draft –; writing – review and editing –. J.I.: Conceptualization; formal analysis; project administration; validation; supervision; visualization; writing – original draft –; writing – review and editing –. D.J.C.: Investigation; validation. D.L-M., R.P-S. and F.A-S.: Investigation; methodology; validation. C.T.: Investigation; validation; resources. M.L.V-P., M.G., A.B., A.S-C., and A.Q-P.: Investigation; validation. A.D. and F.S-C.: Conceptualization; resources. J.J.: Conceptualization; resources; writing – review and editing –. J.L.P.: Conceptualization; methodology; validation; resources; writing – review and editing –. D.F-R.: Conceptualization; Investigation; methodology; validation; resources; writing – review and editing –. P.M-C. and J.M.R.: Conceptualization; formal analysis; funding acquisition; project administration; resources; supervision; visualization; writing – original draft –; writing – review and editing –.

Competing interests

The authors declare no competing interests.

Additional information

Supplementary information The online version contains supplementary material available at https://doi.org/10.1038/s41467-024-52809-1.

Correspondence and requests for materials should be addressed to Pablo Gómez-del Arco, Pura Muñoz-Cánoves or Juan Miguel Redondo.

Peer review information *Nature Communications* thanks the anonymous reviewers for their contribution to the peer review of this work. A peer review file is available.

Reprints and permissions information is available at http://www.nature.com/reprints

Publisher's note Springer Nature remains neutral with regard to jurisdictional claims in published maps and institutional affiliations.

¹Institute for Rare Diseases Research, Instituto de Salud Carlos III (ISCIII). Majadahonda, Madrid, Spain. ²Gene Regulation in Cardiovascular Remodelling and Inflammation Laboratory, Centro Nacional de Investigaciones Cardiovasculares Carlos III (CNIC), Madrid, Spain. ³Centro de Investigación Biomédica en Red de Enfermedades Cardiovasculares (CIBERCV), Madrid, Spain. ⁴Altos Labs, Inc., San Diego Institute of Science, San Diego, CA, USA. ⁵Tissue Regeneration Laboratory, Centro Nacional de Investigaciones Cardiovasculares Carlos III (CNIC), Madrid, Spain. ⁶Bioinformatics Unit, Centro Nacional de Investigaciones Cardiovasculares Carlos III (CNIC), Madrid, Spain. ⁷Intercellular Signaling in Cardiovascular Development and Disease Laboratory, Centro Nacional de

Investigaciones Cardiovasculares Carlos III (CNIC), Madrid, Spain. [8]Cardiac Arrhythmia Laboratory, Centro Nacional de Investigaciones Cardiovasculares Carlos III (CNIC), Madrid, Spain. [9]Genomics Unit, Centro Nacional de Investigaciones Cardiovasculares Carlos III (CNIC), Madrid, Spain. [10]Novel Arrhythmogenic Mechanisms Program, Centro Nacional de Investigaciones Cardiovasculares Carlos III (CNIC), Madrid, Spain. [11]University of Michigan, Ann Arbor, MI, USA. [12]Cardiovascular Institute, Instituto de Investigación Sanitaria del Hospital Clínico San Carlos (IdISSC), Madrid, Spain. [13]Department of Experimental & Health Sciences, University Pompeu Fabra (UPF)/CIBERNED, Barcelona, Spain. [14]Catalan Institution for Research and Advanced Studies (ICREA), Barcelona, Spain. [15]Cell-Cell Communication & Inflammation Unit, Centro de Biología Molecular Severo Ochoa (CBMSO), Consejo Superior de Investigaciones Científicas-Universidad Autónoma de Madrid, Madrid, Spain. [16]Present address: Microscopy and Dynamic Imaging Unit, Centro Nacional de Investigaciones Cardiovasculares Carlos III (CNIC), Madrid, Spain. [17]Present address: Center for Stem Cells and Organoid Medicine (CuSTOM), Cincinnati Children's Hospital Medical Center, Cincinnati, OH, USA. [18]Present address: Department of Medical Biochemistry and Biophysics, Karolinska Institute, Stockholm, Sweden. ✉e-mail: pgomez@isciii.es; pmunozcanoves@altoslabs.com; jmredondo@cbm.csic.es